

This is a self-archived version of an original article. This version may differ from the original in pagination and typographic details.

Author(s): Geng, Zhuoran; Maasilta, Ilari J.

Title: Acoustic wave tunneling across a vacuum gap between two piezoelectric crystals with arbitrary symmetry and orientation

Year: 2022

Version: Published version

Copyright: © 2022 American Physical Society

Rights: CC BY 4.0

Rights url: <https://creativecommons.org/licenses/by/4.0/>

Please cite the original version:

Geng, Z., & Maasilta, I. J. (2022). Acoustic wave tunneling across a vacuum gap between two piezoelectric crystals with arbitrary symmetry and orientation. *Physical Review Research*, 4(3), Article 033073. <https://doi.org/10.1103/PhysRevResearch.4.033073>

Acoustic wave tunneling across a vacuum gap between two piezoelectric crystals with arbitrary symmetry and orientation

Zhuoran Geng^{✉*} and Ilari J. Maasilta^{✉†}

Nanoscience Center, Department of Physics, University of Jyväskylä, P. O. Box 35, FIN-40014 Jyväskylä, Finland



(Received 24 March 2022; accepted 27 June 2022; published 25 July 2022)

It is not widely appreciated that an acoustic wave can “jump” or “tunnel” across a vacuum gap between two piezoelectric solids, nor has the general case been formulated or studied in detail. Here, we remedy that situation, by presenting a general formalism and approach to study such an acoustic tunneling effect between two arbitrarily oriented anisotropic piezoelectric semi-infinite crystals. The approach allows one to solve for the reflection and transmission coefficients of all the partial-wave modes, and is amenable to practical numerical or even analytical implementation, as we demonstrate by a few chosen examples. The formalism can be used in the future for quantitative studies of the tunneling effect in connection not only with the manipulation of acoustic waves, but with many other areas of physics of vibrations such as heat transport, for example.

DOI: [10.1103/PhysRevResearch.4.033073](https://doi.org/10.1103/PhysRevResearch.4.033073)

I. INTRODUCTION

Acoustic waves in solids (also known as elastic waves) have many applications ranging from acoustic wave filters for mobile phones, mechanical resonators for sensors, acousto-optical modulators for optical signal processing, to ultrasonic imaging devices, to name a few [1]. They are often generated with the help of piezoelectric (PE) transducers, converting an electrical signal to an acoustic wave, as piezoelectricity couples acoustic deformations and electric fields [2,3]. This also means that the elastic waves in piezoelectric materials are not purely elastic but contain electric waves as a by-product. To be more descriptive, such waves are sometimes also called acoustoelectric or electroacoustic waves. The main very well understood effect of piezoelectricity on the propagation of acoustic waves is that the acoustic velocities are slightly modified, due to the piezoelectric “stiffening” of the effective elastic constants for wave propagation [2,3].

However, when considering wave transmission and reflection problems, another intriguing and much less widely known effect due to piezoelectricity can happen: a bulk elastic wave can be transmitted across a vacuum gap between two piezoelectric solids. This transmission is not possible for purely elastic waves, which by definition cannot exist in vacuum, but is made possible by the evanescent electric-field components of the electroacoustic waves extending into the vacuum gap. The effect works for gap sizes of the order of the acoustic wavelength, which is much longer than the length scale of

other possible mechanisms that can couple bulk acoustic wave energy across vacuum gaps in the nanometer to subnanometer scale (such as van der Waals, Casimir, and electrostatic interactions discussed in the context of heat transfer, see Refs. [4–9]). As such, the phenomenon is highly analogous to quantum-mechanical tunneling of a particle through a classically forbidden region, and for this reason, we also call this effect “acoustic wave tunneling” or “phonon tunneling,” terminology that was already introduced by others [7–11].

To our knowledge, acoustic wave tunneling mediated by piezoelectricity was first discussed theoretically by Kaliski [12] for the case of horizontally polarized shear (SH) waves in a cubic piezoelectric crystal in the limit of zero gap width. Later, in an important seminal work, Balakirev and Gorchakov [13] extended the calculations for the same SH wave mode for finite gap widths (with the cubic axes aligned with the surfaces). They also provided results for hexagonal crystals with the c_6 -symmetry axis oriented parallel to the surfaces, still considering only the SH wave mode, and plotted examples for the transmission coefficient vs incident angle for $\text{Bi}_{12}\text{GeO}_{20}$ (cubic) and LiIO_3 (hexagonal). An important result of that study was that the transmission coefficient was shown to be large and even approaching unity for angles close to glancing incidence. An experimental study by the same authors [10] with ultrasound ($f = 15$ MHz) using LiIO_3 crystals confirmed the phenomenon with observed transmission coefficients up to ≈ 0.5 .

These early studies used the standard piezoelectrically stiffened elasticity theory [3,14] and were focused on finding explicit solutions, available only for the highest symmetry crystal orientations and for the simplest wave modes, therefore providing only expressions with no generality.

Much more recently, Prunnila and Meltaus revisited the topic in the context of thermal transport using a scattering matrix approach [11] and provided results for energy transmission coefficients as a function of the angle of incidence and wave vector. However, their approach assumed isotropic

*zhgeng@jyu.fi

†maasilta@jyu.fi

properties of the materials, a simplified single component piezoelectric tensor, no PE stiffening, and the results were limited to a single symmetry direction of the “crystal.” Within these approximations only two modes contribute.

On the other hand, to study anisotropic piezoelectric insulators more generally, Barnett and Lothe [15,16] extended the so-called sextic Stroh formalism, an elegant and mathematically powerful tool to analyze anisotropic elasticity [17–20], to an eight-dimensional framework for arbitrary anisotropic piezoelectric crystals. This extended Stroh formalism was further developed by several authors [21–26] and has been successfully applied from the analysis of reflection of bulk electroacoustic waves [21–23] and anisotropic piezoelectric surface acoustic waves (SAW) [16,27,28] to the gap waves (GW) [29–31], which are surface waves guided and coupled by a gap between two piezoelectric surfaces [32,33]. It has also been used in material science applications for piezoelectric ceramics and composites [34–36] and recently [37] also to study the control SAW propagation using piezoelectric phononic crystals [38].

Even though the framework of extended piezoelectric Stroh formalism was developed some time ago, only a limited number of investigations have been carried out to study the phenomenon of bulk acoustic wave tunneling. Al’shits *et al.* [29] introduced formally a general solution of reflection and transmission coefficient for an incident slow quasitransverse bulk wave. Later, Darinskii developed this framework further [39,40] and investigated the reflection and transmission mediated by the leaky gap wave [31]. In these studies, only single transmitted bulk wave mode was considered, and the resonance conditions of the leaky gap waves were usually applied.

The purpose of this work is to demonstrate a general formalism and solution for transmission of elastic waves across a vacuum gap that is applicable to any incident bulk wave mode in any anisotropic crystallographic orientation. Furthermore, an alternative approach to the direct solution will be presented. In this method, the scattering problems of semi-infinite piezoelectric half-spaces are solved independently for both crystals using the extended Stroh formalism, and the reflection and transmission coefficients of the tunneling are acquired with a simple factor, which is determined from multiple reflections of evanescent electric waves inside the vacuum gap. To our knowledge, such an interpretation of acoustic wave tunneling has not been discussed in literature, although the multiple reflection picture has been widely adopted in the field of near-field electromagnetic wave tunneling [41–43].

This work is organized as follows: We first briefly introduce the main aspects of the extended Stroh formalism for plane interface scattering problems using generally applicable coordinate setup and plane-wave functions in Sec. II. The tunneling problem for the plane-plane geometry is then solved in Sec. III, first by directly applying the boundary conditions to the Stroh eigenfunctions, then followed by the alternative approach of using multiple reflection factor. In Sec. IV, we then present a few illustrative examples: first an analytical solution for a hexagonal crystal with a high-symmetry orientation derived using both methods, and finally numerical calculations of tunneling transmission coefficients for a couple of different crystallographic cuts of a hexagonal crystal

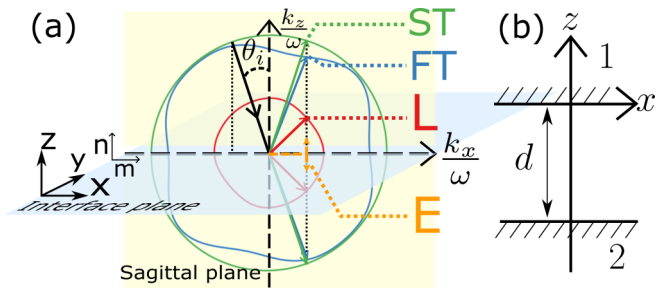


FIG. 1. (a) Schematic of the single interface scattering problem with the coordinate system used, with the interface plane at $z = 0$ and the sagittal plane at $y = 0$. The scattering and mode conversions of an incident bulk slow transverse (ST) wave from the angle θ_i are shown, with a hypothetical set of slowness surfaces. \mathbf{m} and \mathbf{n} are the unit vectors of the x axis and z axis. Under the quasistatic approximation, four wave modes are shown: longitudinal (L), fast transverse (FT), slow transverse (ST), and quasistatic electric potential (E). (b) Two piezoelectric media 1, 2 are separated by a vacuum gap of width d .

in different orientations. At the end in Sec. V, we present conclusions and outlook on the applications of this study.

II. EXTENDED STROH FORMALISM FOR SCATTERING PROBLEMS

We consider acoustic waves within the continuum anisotropic linear elasticity theory. A bulk acoustic plane wave with a wave vector \mathbf{k} in an anisotropic piezoelectric medium using Cartesian coordinates $\mathbf{r} = [x, y, z]^T$ ($[\dots]^T$ stands for transposition) is incident on an interface plane $\mathbf{n} \cdot \mathbf{r} = z = 0$ between two media, with a plane of incidence (sagittal plane) $(\mathbf{n} \times \mathbf{m}) \cdot \mathbf{r} = y = 0$, where \mathbf{n} is the unit normal vector of the interface plane and \mathbf{m} the unit vector parallel to the interface and sagittal planes. With our coordinate system, they are the unit vectors of the z axis and x axis, respectively [see Fig. 1(a)]. Without losing generality, we always consider that the incident bulk wave has a positive x component of the wave vector $k_x > 0$ and propagates in the sagittal plane (the wave vector is contained in the plane), but the sagittal plane has a rotational degree of freedom with respect to the normal of interface plane (z axis).¹ The piezoelectric medium is characterized by its density ρ , piezoelectric stress tensor e_{iL} , elastic stiffness tensor at constant electric field c_{KL}^E , and electric permittivity tensor at constant strain ϵ_{ij}^S , where $i, j = x, y, z$ are the Cartesian coordinate indices and $K, L = 1, \dots, 6$ are the abbreviated Voigt indices.

The sound velocities $v = \omega/k$ are typically more than four orders of magnitude slower than the speed of light, therefore it is possible and customary to apply the quasistatic approximation [3] to the piezoelectric scattering problems, ignoring the magnetic field. Under such conditions, the propagation of

¹The sagittal plane has a rotational degree of freedom with respect to the normal of the interface plane (azimuth angle), which is equivalent to the rotation of the crystal azimuth angle φ . For the sake of simplicity and to avoid the duplication of the effect of this degree of freedom, we unambiguously take into account the azimuth angle by the rotation of the crystal (see Appendix F).

a time-harmonic plane wave $\propto \exp(-i\mathbf{k} \cdot \mathbf{r} + i\omega t)$ with wave vector \mathbf{k} and angular frequency ω is governed by the elastic equation of motion $\nabla \cdot \boldsymbol{\sigma} = \rho \partial^2 \mathbf{u} / \partial t^2$ and just one of the Maxwell's equations (Gauss's law) $\nabla \cdot \mathbf{D} = 0$, which together with the piezoelectric constitutive relations read in the matrix notation [3]:

$$\begin{aligned} ik_{iK} \sigma_K &= \rho \omega^2 u_i, \\ -ik_i D_i &= 0, \\ \sigma_K &= -ic_{KL}^E k_{Lj} u_j - ie_{Kj} k_j \Phi, \\ D_i &= -ie_{iL} k_{Lj} u_j + i\epsilon_{ij}^S k_j \Phi, \end{aligned} \quad (1)$$

where $\boldsymbol{\sigma}$, \mathbf{u} , \mathbf{D} are the elastic stress, mechanical displacement, and electric displacement fields, respectively, Φ is the electric potential, and k_{iK} is a 3×6 matrix defined by the wave-vector components [3] (see Appendix A for more details). As usual, repeated indices are summed.

An incident plane wave is scattered into a linear combination of partial waves at the interface, which are either reflected or transmitted, and can also be inhomogeneous modes. [An example where three reflected and transmitted homogeneous bulk acoustic waves and an inhomogeneous electric potential wave are generated is depicted in Fig. 1(a).] The general solutions of such partial waves that satisfy the governing equations can be written [21–23] as

$$\begin{aligned} \mathbf{u} &= \sum_{\alpha} b_{\alpha} \mathbf{A}_{\alpha} e^{-ik_x(x+p_{\alpha}z)+i\omega t}, \\ \Phi &= \sum_{\alpha} b_{\alpha} \phi_{\alpha} e^{-ik_x(x+p_{\alpha}z)+i\omega t}, \\ \mathbf{n} \cdot \boldsymbol{\sigma} &= ik_x \sum_{\alpha} b_{\alpha} \mathbf{L}_{\alpha} e^{-ik_x(x+p_{\alpha}z)+i\omega t}, \\ \mathbf{n} \cdot \mathbf{D} &= ik_x \sum_{\alpha} b_{\alpha} D_{\alpha}^n e^{-ik_x(x+p_{\alpha}z)+i\omega t}, \end{aligned} \quad (2)$$

in which \mathbf{A}_{α} , ϕ_{α} , \mathbf{L}_{α} , D_{α}^n are normalized constants describing the displacement (polarization vector), the electric potential, the traction force and the normal projection of the electric displacement of a partial wave mode α , respectively. b_{α} is the dimensionless amplitude of the partial wave, and $p \equiv k_z/k_x$ where k_z and k_x are the normal and parallel components of the \mathbf{k} vector. To avoid redundant writing in expressions, we omit from now on the common phase factor $\exp(-ik_x x + i\omega t)$ shared by all solutions.

With the above partial-wave formulation, the solution of the governing equations (1) reduces to determining the eigenvalues p_{α} and eigenvectors $\boldsymbol{\xi}_{\alpha}$ of an eight-dimensional eigenvalue problem [15,16] with a 8×8 real matrix N :

$$N(v_x) \boldsymbol{\xi}_{\alpha} = p_{\alpha} \boldsymbol{\xi}_{\alpha}, \quad (3)$$

where the matrix $N(v_x)$ depends on the phase velocity along the interface $v_x \equiv \omega/k_x$, a conserved quantity due to continuity conditions on the boundary, and the orientation and material of the crystal. The eight-component eigenvector for mode α is defined as $\boldsymbol{\xi}_{\alpha} = [\mathbf{A}_{\alpha}, \phi_{\alpha}, \mathbf{L}_{\alpha}, D_{\alpha}^n]^T$. The derivation of Eq. (3) with the detailed definition of $N(v_x)$ is presented in Appendix B.

The matrix N also satisfies the symmetry relation $(\hat{\mathbf{T}}N)^T = \hat{\mathbf{T}}N$, where the 8×8 matrix $\hat{\mathbf{T}}$ is given by

$$\hat{\mathbf{T}} = \begin{bmatrix} \hat{\mathbf{0}} & \hat{\mathbf{I}} \\ \hat{\mathbf{I}} & \hat{\mathbf{0}} \end{bmatrix},$$

with $\hat{\mathbf{I}}$ and $\hat{\mathbf{0}}$ the 4×4 unit and zero matrices, respectively [17,18,44]. This relation provides an orthonormalization condition:

$$\boldsymbol{\xi}_{\alpha}^T \hat{\mathbf{T}} \boldsymbol{\xi}_{\beta} = \delta_{\alpha\beta}, \quad \alpha, \beta = 1, \dots, 8, \quad (4)$$

where $\delta_{\alpha\beta}$ is the Kronecker delta and ensures a unique and complete set of solutions for the extended Stroh eigenfunction.²

At this point it is good to point out that the above ‘‘Stroh-normalization’’, widely used in literature as it is, does not keep the physical units (as $\boldsymbol{\xi}_{\alpha}^T \hat{\mathbf{T}} \boldsymbol{\xi}_{\alpha}$ has units of force), but introduces computationally useful ‘‘Stroh units.’’ This is not a problem, as the units cancel out in the end if transmission and reflection amplitudes are the observables to be calculated.

Totally eight partial-wave mode solutions can be obtained from Eq. (3), containing complex eigenvalues $p_{\alpha} = p'_{\alpha} + ip''_{\alpha}$ and the associated eigenvectors $\boldsymbol{\xi}_{\alpha}$ with $\alpha = 1, \dots, 8$ (with p'_{α} denoting the real part and p''_{α} the imaginary part). These partial waves can be either homogeneous plane waves ($p''_{\alpha} = 0$) or inhomogeneous waves ($p''_{\alpha} \neq 0$). For an inhomogeneous wave mode, the scattering direction of the wave is determined by the imaginary part of the eigenvalue such that if $p''_{\alpha} > 0$ ($p''_{\alpha} < 0$) the wave is transmitted (reflected), to ensure decaying solutions at infinity. For a plane-wave mode, the direction of the power flow normal to the interface is examined. By investigating the time-averaged acoustic Poynting vector component normal to the interface [21]

$$P_{n\alpha} \equiv \mathbf{n} \cdot \mathbf{P}_{AV,\alpha} = -\frac{\omega k_x}{4} |b_{\alpha}|^2 \boldsymbol{\xi}_{\alpha}^T \hat{\mathbf{T}} \boldsymbol{\xi}_{\alpha}^*, \quad (5)$$

one can determine which wave mode is transmitted ($P_{n\alpha} < 0$) or reflected ($P_{n\alpha} > 0$).

If Stroh-normalization is used, Eq. (5) simplifies even further for the bulk modes. For them, the eigenvalues p_{α} are real, which means that the eigenvectors are real as well, $\boldsymbol{\xi}_{\alpha}^* = \boldsymbol{\xi}_{\alpha}$, as N is real. We then have $\boldsymbol{\xi}_{\alpha}^T \hat{\mathbf{T}} \boldsymbol{\xi}_{\alpha}^* = \boldsymbol{\xi}_{\alpha}^T \hat{\mathbf{T}} \boldsymbol{\xi}_{\alpha} = 1$, and see from Eq. (5) that the power transmission and reflection coefficients (ratios of Poynting vector normal components) are simply given by the ratio $|b_{\alpha}/b_{in}|^2$. This is one justification for the usefulness of the used Stroh normalization.

²The above results are strictly true only if N is nondegenerate (has a nonzero determinant). Slightly modified eigenvectors and normalization conditions have been determined in the opposite case [28] taking place at the exact conditions for a critical angle (transonic state), where the reflected bulk wave carries energy only along the interface. Our discussion is meant for the general case to facilitate numerical computation, thus these conditions are special cases that do not have to be considered here, as numerical computation can be done very close to the exact conditions.

III. BULK ACOUSTIC WAVE TUNNELING ACROSS A VACUUM GAP

To formulate a generalized expression for bulk acoustic wave tunneling across a vacuum gap between two adjacent piezoelectric solids, we consider a geometry which consists of two parallel semi-infinite piezoelectric half spaces (medium 1 and medium 2) separated by a vacuum gap of distance d , as shown in Fig. 1(b). Our modeling is not applicable for nonpiezoelectric solids, or in situations where one or more of the dimensions of the solids are smaller than the acoustic wavelength in question (breakdown of the bulk wave assumption), or when the gap size or solid dimensions are in the atomic length scale (breakdown of continuum elasticity). The incident wave is propagating towards the gap from the positive z -coordinate direction in the sagittal plane, and the two solid-vacuum interfaces are located at $\mathbf{n} \cdot \mathbf{r} = 0$ and $\mathbf{n} \cdot \mathbf{r} = -d$.

For a given incident wave propagating in a given crystal orientation, the wave vector and phase velocity components along the interface (k_x and v_x) are known. Therefore, the unknowns left in the partial-wave solutions in Eqs. (2) are the eigenvectors ξ_α and eigenvalues p_α of the Stroh eigenequation (3), as well as the amplitude factors b_α . The eigenvectors and eigenvalues can readily be solved with the knowledge of the material, the crystallographic orientation and v_x , whereas the determination of b_α requires solving the boundary conditions of the solid-vacuum interfaces.

We assume for this study that both interfaces are mechanically free and without electrodes or net charge density on the surface, i.e., electrically free. For such a case, there are conditions for the continuity of the electric potential and the normal component of the electric displacement, giving for the boundary conditions

$$\begin{aligned} \Phi^{(i)} &= \Phi_V, \\ \mathbf{n} \cdot \mathbf{D}^{(i)} &= \mathbf{n} \cdot \mathbf{D}_V, \\ \mathbf{n} \cdot \boldsymbol{\sigma}^{(i)} &= \mathbf{0}, \end{aligned} \quad (6)$$

in which the superscript $i = 1, 2$ indicates the medium index and the subscript V represents the fields in the vacuum gap.

In the vacuum region, the electric potential wave must satisfy the Laplace equation $\nabla^2 \Phi_V = 0$, which for the plane waves leads to the condition $k_x^2 + k_z^2 = 0$. Thus, it can be expressed in terms of two partial wave modes with $k_z = \pm ik_x$. Following the form of the general solutions for the electric potential in Eq. (2) leads to a solution with decaying and increasing exponentials [omitting the common phase factor $\exp(-ik_x x + i\omega t)$]

$$\Phi_V = b_{V+} \phi_{V+} e^{k_x z} + b_{V-} \phi_{V-} e^{-k_x z}, \quad (7)$$

and the normal component of the vacuum electric displacement can then be calculated directly from $\mathbf{D}_V = -\epsilon_0 \nabla \cdot \Phi_V$, giving

$$\mathbf{n} \cdot \mathbf{D}_V = -\epsilon_0 k_x b_{V+} \phi_{V+} e^{k_x z} + \epsilon_0 k_x b_{V-} \phi_{V-} e^{-k_x z}. \quad (8)$$

From the form of solutions above, the analogy with quantum-mechanical tunneling is apparent.

Comparing the result for the electric displacement in Eq. (8) with the definitions of the Stroh formalism, Eqs. (2), we see that the components for the electric displacement $D_{V\pm}$

and for the potential $\phi_{V\pm}$ satisfy a simple relation $D_{V\pm} = \pm i\epsilon_0 \phi_{V\pm}$. In addition, we have $\phi_{V\pm} = 1/\sqrt{\pm 2i\epsilon_0}$, as can be readily calculated from the Stroh-normalization condition $2\phi_{V\pm} D_{V\pm} = 1$ obtained from Eq. (4) by setting the vacuum eigenvector components associated with the displacement and traction force to zero: $\mathbf{A}_{V\pm} = \mathbf{0}, \mathbf{L}_{V\pm} = \mathbf{0}$.

By inserting the general solutions of Eqs. (2), (7), and (8) into the boundary conditions in Eqs. (6), we obtain two sets of linear equations to express the boundary conditions at both interfaces as

$$\begin{aligned} b_{in}^{(1)} \mathbf{U}_{in}^{(1)} + \sum_{\alpha=1}^4 b_\alpha^{(1)} \mathbf{U}_\alpha^{(1)} &= b_{V+} \mathbf{U}_{V+} + b_{V-} \mathbf{U}_{V-}, \\ \sum_{\alpha=1}^4 \tilde{b}_\alpha^{(2)} \mathbf{U}_\alpha^{(2)} &= b_{V+} \mathbf{U}_{V+} e^{-k_x d} + b_{V-} \mathbf{U}_{V-} e^{k_x d}, \end{aligned} \quad (9)$$

in which we introduce a 5×1 column vector $\mathbf{U}_\gamma^{(i)} = [\phi_\gamma^{(i)}, D_\gamma^{n,(i)}, \mathbf{L}_\gamma^{(i)}]^T$ for the wave mode $\gamma = in, \alpha$, where the subscript in indicates the incident wave mode, $\alpha = 1, \dots, 4$ corresponds to the four physically allowed wave modes in the corresponding media $i = 1, 2$ (the reflected and transmitted modes, respectively), and $\tilde{b}_\alpha^{(2)} \equiv b_\alpha^{(2)} \exp(ip_\alpha^{(2)} k_x d)$. As $\mathbf{U}_\gamma^{(i)}$ are known and defined by the Stroh eigenvectors (more explicit expressions can be found in Appendix C), Eqs. (9) can be used to solve for the partial-wave amplitudes $b_\alpha^{(i)}, b_{V\pm}$, giving us finally the transmission and reflection amplitude coefficients $t_\alpha^{(2)} \equiv \tilde{b}_\alpha^{(2)}/b_{in}^{(1)}$ and $r_\alpha^{(1)} \equiv b_\alpha^{(1)}/b_{in}^{(1)}$.

We have considered two approaches to solve Eqs. (9): First, by directly solving the combined boundary conditions of both interfaces with matrix algebra, and second, by using a multiple reflection factor to connect the separate solutions on each interface. Both approaches are discussed in the following and give identical results. The choice of the method should be based on which parameters are to be varied: In the case where the incident wave is a variable, the first combined boundary-condition method is more efficient, whereas if the gap size is a variable, the second multiple reflection amplitude method is more practical, as will become clearer below.

A. Combined boundary conditions approach

In the first approach, where the boundary conditions are solved directly, we introduce two 8×5 matrices \mathbf{M}_1 and \mathbf{M}_2 :

$$\mathbf{M}_1 = \begin{bmatrix} \mathbf{V}_1^{-1} & \hat{\mathbf{O}}_{(2 \times 3)} \\ \hat{\mathbf{O}}_{(3 \times 2)} & \hat{\mathbf{I}}_{(3)} \\ \hat{\mathbf{O}}_{(3 \times 2)} & \hat{\mathbf{O}}_{(3 \times 3)} \end{bmatrix}, \quad \mathbf{M}_2 = \begin{bmatrix} \mathbf{V}_2^{-1} & \hat{\mathbf{O}}_{(2 \times 3)} \\ \hat{\mathbf{O}}_{(3 \times 2)} & \hat{\mathbf{O}}_{(3 \times 3)} \\ \hat{\mathbf{O}}_{(3 \times 2)} & \hat{\mathbf{I}}_{(3)} \end{bmatrix}, \quad (10)$$

in which $\hat{\mathbf{O}}_{(m \times n)}$ and $\hat{\mathbf{I}}_{(m)}$ are the $m \times n$ zero matrix and the $m \times m$ identity (unit) matrix. $\mathbf{V}_1, \mathbf{V}_2$ are 2×2 matrices depending only on the wave-vector component k_x along the interface and the size of vacuum gap d :

$$\mathbf{V}_1 = \begin{bmatrix} \phi_{V+} & \phi_{V-} \\ D_{V+} & D_{V-} \end{bmatrix}, \quad \mathbf{V}_2 = \begin{bmatrix} \phi_{V+} e^{-k_x d} & \phi_{V-} e^{k_x d} \\ D_{V+} e^{-k_x d} & D_{V-} e^{k_x d} \end{bmatrix},$$

as we recall that both $D_{V\pm}$ and $\phi_{V\pm}$ are simply set by the vacuum permittivity ϵ_0 : $D_{V\pm} = \pm i\epsilon_0 \phi_{V\pm}, \phi_{V\pm} = 1/\sqrt{\pm 2i\epsilon_0}$.

With the above definitions, the boundary conditions in Eqs. (9) can then be written in the following compact form (the detailed derivation can be found in Appendix C):

$$\mathbf{M}[b_1^{(1)}, \dots, b_4^{(1)}, \tilde{b}_1^{(2)}, \dots, \tilde{b}_4^{(2)}]^T = -\mathbf{M}_1 \mathbf{U}_{in}^{(1)} b_{in}^{(1)},$$

where \mathbf{M} is a 8×8 matrix constructed by joining four ($\alpha = 1 \dots 4$) $\mathbf{M}_1 \mathbf{U}_\alpha^{(1)}$ and four $-\mathbf{M}_2 \mathbf{U}_\alpha^{(2)}$ 8×1 column vectors together as

$$\mathbf{M} = [\mathbf{M}_1 \mathbf{U}_1^{(1)}, \mathbf{M}_1 \mathbf{U}_2^{(1)}, \mathbf{M}_1 \mathbf{U}_3^{(1)}, \mathbf{M}_1 \mathbf{U}_4^{(1)}, \\ -\mathbf{M}_2 \mathbf{U}_1^{(2)}, -\mathbf{M}_2 \mathbf{U}_2^{(2)}, -\mathbf{M}_2 \mathbf{U}_3^{(2)}, -\mathbf{M}_2 \mathbf{U}_4^{(2)}]. \quad (11)$$

All the reflection coefficients $r_\alpha^{(1)} \equiv b_\alpha^{(1)}/b_{in}^{(1)}$ in medium 1 and all the transmission coefficients $t_\alpha^{(2)} \equiv \tilde{b}_\alpha^{(2)}/b_{in}^{(1)}$ in medium 2 of the partial-wave amplitudes can therefore be solved simultaneously as

$$[r_1^{(1)}, \dots, r_4^{(1)}, t_1^{(2)}, \dots, t_4^{(2)}]^T = -\mathbf{M}^{-1} \mathbf{M}_1 \mathbf{U}_{in}^{(1)}. \quad (12)$$

We remark that, with the given materials, crystallographic orientations, the size of the vacuum gap and the frequency, the matrices \mathbf{M} and \mathbf{M}_1 depend only on the wave-vector component k_x along the interface, which is a *conserved quantity* for all partial-wave modes in a scattering problem. The detailed information about the incident wave, such as the normal component of the wave vector k_z and the polarization \mathbf{A}_{in} , are defined separately in the column vector $\mathbf{U}_{in}^{(1)}$. This means that the choice of the incident wave mode does not influence the calculation \mathbf{M} and \mathbf{M}_1 , therefore those matrices are only computed once for a given k_x , and the reflection and transmission coefficients for all the incident modes can readily be obtained simply by changing $\mathbf{U}_{in}^{(1)}$.

In contrast, in the approach described by Ref. [29] in which Cramer's rule is used, the matrices used in equations (38) and (39) of Ref. [29] have to be reconstructed and calculated each time a new incident wave mode is given. This is because the common columns of these matrices should be the eigenvector solutions of all the transmitted wave modes except the incident mode, to ensure the columns of the fully constructed matrices are linearly independent. Furthermore, Cramer's rule used in Ref. [29] requires computation of $n + 1$ determinants to solve n linear equations, which is considered computationally inefficient compared with the single matrix inversion used in Eq. (12) in our approach.

B. Multiple reflection approach

In the second, alternative approach, the reflected and transmitted waves in both media can be considered to be coupled by a superposition of multiply reflected evanescent electric potential waves in the vacuum gap. A similar picture has been adopted before in the description of the analogous "photon tunneling", in other words the frustrated total internal reflection phenomenon for electromagnetic waves in optics [45,46].

In this approach, we define two 5×2 scattering matrices $\mathbf{S}^{(1)}$ and $\mathbf{S}^{(2)}$ for the two vacuum-solid interfaces (connecting the incoming and outgoing partial wave amplitudes for all modes), calculated separately for each interface [for the definitions, see Appendix D, Fig. 6 and Eq. (D1)]. These scattering matrices are generalized in the sense that they include evanescent modes, in particular the two evanescent vacuum

gap modes. As shown in Appendix D, the resulting scattering matrices are

$$\mathbf{S}^{(1)} = \begin{bmatrix} \bar{\mathbf{r}}^{(1)} & \bar{\mathbf{t}}^{(1)} \\ \bar{\mathbf{t}}_V^{(1)} & \bar{\mathbf{r}}_V^{(1)} \end{bmatrix} \\ = [\mathbf{U}_1^{(1)}, \dots, \mathbf{U}_4^{(1)}, -\mathbf{U}_{V_+}]^{-1} [-\mathbf{U}_{in}^{(1)}, \mathbf{U}_{V_-}], \\ \mathbf{S}^{(2)} = \begin{bmatrix} \bar{\mathbf{r}}^{(2)} & \bar{\mathbf{t}}^{(2)} \\ \bar{\mathbf{t}}_V^{(2)} & \bar{\mathbf{r}}_V^{(2)} \end{bmatrix} \\ = [\mathbf{U}_1^{(2)}, \dots, \mathbf{U}_4^{(2)}, -\mathbf{U}_{V_-}]^{-1} [-\mathbf{U}_{in}^{(2)}, \mathbf{U}_{V_+}], \quad (13)$$

where $\bar{\mathbf{r}}^{(i)} = [\bar{r}_1^{(i)}, \dots, \bar{r}_4^{(i)}]^T$ are the reflection amplitude coefficients into modes $\alpha = 1, \dots, 4$ of the incoming wave mode from medium $i = 1, 2$, $\bar{\mathbf{r}}_V^{(i)}$ the reflection amplitude coefficient from medium i of an incoming vacuum mode, $\bar{\mathbf{t}}^{(i)} = [\bar{t}_1^{(i)}, \dots, \bar{t}_4^{(i)}]^T$ the transmission amplitude coefficients of an incoming vacuum mode into wave modes $\alpha = 1, \dots, 4$ of medium i , and finally, $\bar{\mathbf{t}}_V^{(i)}$ the transmission amplitude coefficient of the incoming wave mode from medium i into a vacuum mode. To avoid confusion with the coupled scattering coefficients calculated with the direct approach in Sec. III A [Eq. (12)], we have used bars on the top of the symbols here. These "bare" coefficients describe the scattering of the electroacoustic wave as if there is no second bulk medium and will be used below to construct the total tunneling transmission and reflection coefficients with the help of a multiple reflection factor generated by the vacuum gap.

The total transmission factor consists of sum of partial evanescent waves in the gap that have traversed the gap once, reflected at both interfaces and traversed the gap three times, and so on. We therefore get a geometric series for the total transmission coefficient into mode α , $t_\alpha^{(2)}$ as

$$t_\alpha^{(2)} = \bar{\mathbf{t}}_V^{(1)} e^{-k_x d} \bar{\mathbf{t}}_\alpha^{(2)} + \bar{\mathbf{t}}_V^{(1)} \bar{\mathbf{r}}_V^{(1)} \bar{\mathbf{r}}_V^{(2)} e^{-3k_x d} \bar{\mathbf{t}}_\alpha^{(2)} \\ + \bar{\mathbf{t}}_V^{(1)} (\bar{\mathbf{r}}_V^{(1)})^2 (\bar{\mathbf{r}}_V^{(2)})^2 e^{-5k_x d} \bar{\mathbf{t}}_\alpha^{(2)} + \dots \\ = \frac{\bar{\mathbf{t}}_V^{(1)} \bar{\mathbf{t}}_\alpha^{(2)} e^{-k_x d}}{1 - \bar{\mathbf{r}}_V^{(1)} \bar{\mathbf{r}}_V^{(2)} e^{-2k_x d}},$$

where an attenuation factor $e^{-k_x d}$ due to the wave path has been included each time wave passes through the gap. We can also calculate the total reflection coefficient the same way. Collecting in both cases the common multiple reflection factor

$$f_m(d) = \frac{e^{-k_x d}}{1 - \bar{\mathbf{r}}_V^{(1)} \bar{\mathbf{r}}_V^{(2)} e^{-2k_x d}}, \quad (14)$$

we arrive at the expressions for the total transmission and reflection coefficients $t_\alpha^{(2)}$ and $r_\alpha^{(1)}$ from the input mode into the mode $\alpha = 1, \dots, 4$ in medium (2) (transmission) or in (1) (reflection):

$$t_\alpha^{(2)} = \bar{\mathbf{t}}_\alpha^{(2)} \bar{\mathbf{t}}_V^{(1)} f_m(d), \quad (15)$$

$$r_\alpha^{(1)} = \bar{\mathbf{r}}_\alpha^{(1)} + \bar{\mathbf{r}}_V^{(2)} \bar{\mathbf{t}}_\alpha^{(1)} \bar{\mathbf{t}}_V^{(1)} f_m(d) e^{-k_x d}. \quad (16)$$

We have checked that the results of the multiple reflection approach are identical to our previously derived scattering coefficients determined using the first, combined boundary conditions approach. The main difference is that in this second

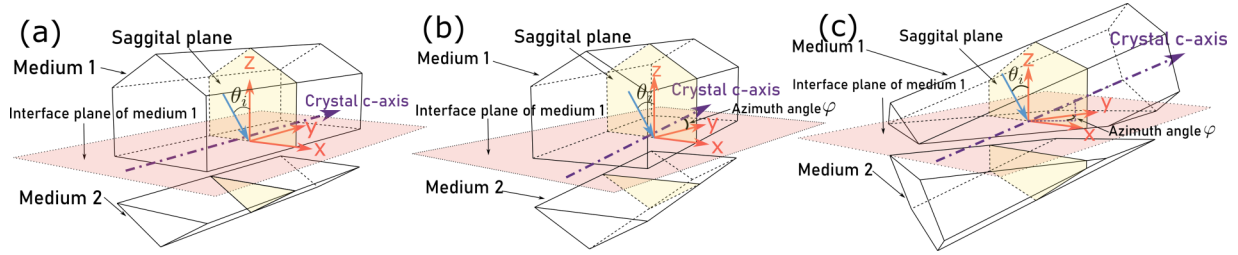


FIG. 2. Wurtzite hexagonal crystal orientations used in the illustrative examples. (a) In the analytical example (Sec. IV A), the vacuum gap is cut through the a plane $[11\bar{2}0]$ of the crystal. The azimuthal angle $\varphi = 0$ and the polarization of the wave is aligned with the crystallographic c axis. (b) In the first numerical example, vacuum gap is also cut through the a plane $[11\bar{2}0]$ of the crystal, while the azimuthal angle is rotated from 0° to 360° with respect to the z axis. (c) In the second numerical example, the vacuum gap is cut through the n plane $[11\bar{2}3]$ of the crystal. The crystallographic c axis is no longer parallel to the interface plane, while the azimuthal angle is rotated from 0° to 360° with respect to the z axis.

approach, the gap distance d is completely separated from the calculation of the matrices. For given materials, crystal orientations and the incident wave, the scattering matrices $\mathbf{S}^{(1)}$ and $\mathbf{S}^{(2)}$ are independent of the gap distance, and the effects of the gap to the scattering coefficients can easily be obtained through the explicit factor $f_m(d)$. This makes the computation as a function of the gap distance easier, as the scattering matrices are computed only once. In addition, the multiple reflection approach provides an alternative physical picture of the phenomenon of tunneling of acoustic waves through a vacuum gap, analogous to the near-field electromagnetic wave “tunneling” (frustrated total internal reflection) [45,46]. To the authors’ knowledge, this multiple reflection picture has not been described in the literature before for the problem of bulk electroacoustic wave tunneling.

IV. ILLUSTRATIVE EXAMPLES

In this section, we provide some example calculations, first for a rare case that is analytically soluble. After that, we provide a limited set of examples of numerical results for a hexagonal ZnO crystal with varying crystal orientation. The results are not meant to be exhaustive, as the main focus of this work is the introduction of the formalism and the workflow how solutions can be obtained.

A. Analytical example for an incident fast transverse bulk wave

Generally speaking, for crystals with arbitrary anisotropy and orientation, it is not possible to obtain simple analytical expressions for the reflection and transmission coefficients for bulk acoustic wave tunneling. However, for some particular incident modes and high-symmetry crystal configurations, analytical solutions can be acquired. In this section, we demonstrate results for such an example: a fast transverse (FT) incident bulk wave scattering from a gap structure between two identical wurtzite hexagonal crystals ($6mm$ symmetry)

with the same crystal orientation. The acoustic polarization direction of the incident wave is aligned with the crystallographic c axis, which is perpendicular to the sagittal plane [see Fig. 2(a)], in other words the c axis is aligned with the solid-vacuum interface planes. With such a high-symmetry configuration, one could also call the incident wave mode a horizontally polarized shear wave (SH).

With the above configuration, there is no mode conversion and only acoustic waves with the same polarization can be excited and scattered [3], therefore the matrix N in the eigenequation (3) simplifies to a 4×4 matrix and the eigenvectors are four-vectors $[u_y, \phi, L_{yz}, D^n]^T$ (for details, see Appendix E):

$$N(v_x) = \begin{bmatrix} 0 & 0 & -\frac{\epsilon_{11}}{\epsilon_{11}c_{44} + e_{15}^2} & \frac{e_{15}}{\epsilon_{11}c_{44} + e_{15}^2} \\ 0 & 0 & \frac{e_{15}}{\epsilon_{11}c_{44} + e_{15}^2} & \frac{c_{44}}{\epsilon_{11}c_{44} + e_{15}^2} \\ c_{44} - \rho v_x^2 & -e_{15} & 0 & 0 \\ -e_{15} & -\epsilon_0 & 0 & 0 \end{bmatrix}. \quad (17)$$

The phase velocity along the interface v_x contained in N can easily be found using the dispersion relation $(c_{44} + e_{15}^2/\epsilon_{11})k^2 = \rho\omega^2$ [3] and the definition of the incident angle θ_i in $v_x = v \sin \theta_i$:

$$v_x^2 = \frac{\epsilon_{11}c_{44} + e_{15}^2}{\epsilon_{11}\rho \sin^2 \theta_i}.$$

A set of four eigenvalues ($p_\alpha = \pm \cot \theta_i$ and $\pm i$) and eigenvectors can be obtained, corresponding to two homogeneous (transverse modes) and two inhomogeneous (evanescent modes) partial waves. In particular, the particle displacement fields vanish in the solutions of inhomogeneous waves, but their stress fields exist. In contrast, for the bulk modes, the electrical displacement fields vanish, but not the electrical potential (Appendix E).

Matrix M can be constructed following our first approach and obtained using straightforward algebra as

$$\mathbf{M} = \frac{1}{2} \begin{bmatrix} -U & i(\epsilon_0 - \epsilon_{11})V & -iUe^{k_x d} & -(\epsilon_0 + \epsilon_{11})Ve^{k_x d} \\ iU & (\epsilon_0 + \epsilon_{11})V & -Ue^{-k_x d} & i(\epsilon_0 - \epsilon_{11})Ve^{-k_x d} \\ -i\sqrt{2\epsilon_{11}}B & -i\sqrt{2i\epsilon_{11}}A & 0 & 0 \\ 0 & 0 & -\sqrt{2\epsilon_{11}}B & -\sqrt{2i\epsilon_{11}}A \end{bmatrix},$$

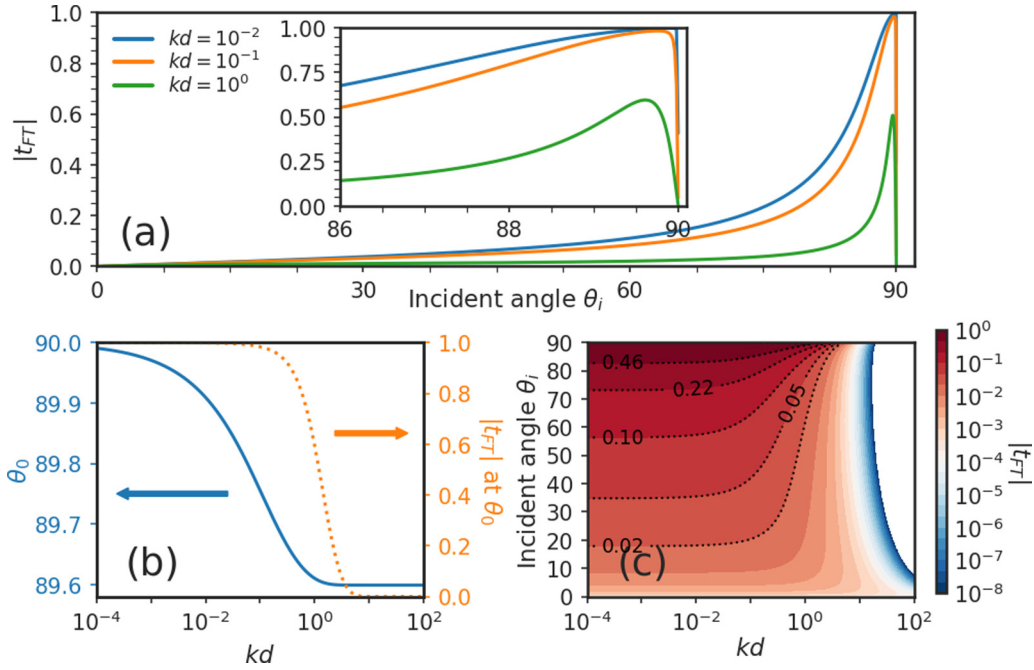


FIG. 3. (a) Dependence of the magnitude of the amplitude transmission coefficients $|t_{FT}|$, from Eq. (19), of a fast transverse wave tunneling between two ZnO crystals aligned as in Fig. 2(a), as a function of the incident angle θ_i , with three different values of $kd = 0.01, 0.1, 1$, where d is the gap width and k the incident wave-vector magnitude. The inset zooms into the glancing angles. (b) Dependence of the peak transmission angle θ_0 (left axis) on kd , with the right axis showing the corresponding $|t_{FT}|$ at θ_0 . (c) Colored contour plot of the magnitude of the transmission coefficient $|t_{FT}|$ in a logarithmic scale versus incident angle θ_i and kd .

where $A = e_{15}/\epsilon_{11}$, $B^2 = (A^2 + c_{44}/\epsilon_{11}) \cot \theta_i$, $\{B \in \Re | B \geq 0\}$, $U = i\sqrt{i\epsilon_0 A}/\sqrt{\epsilon_{11} B}$, and $V = 1/\sqrt{\epsilon_0 \epsilon_{11}}$.

The exact solutions of the reflection and transmission coefficients of the fast transverse partial wave mode can be obtained from Eq. (12):

$$r_{FT} = 2iA^2\epsilon_0 \frac{Q_+ e^{2k_x d} - Q_-}{Q_+^2 e^{2k_x d} - Q_-^2} - i, \quad (18)$$

$$t_{FT} = -\frac{4iA^2 B^2 \epsilon_0 \epsilon_{11} e^{k_x d}}{Q_+^2 e^{2k_x d} - Q_-^2}, \quad (19)$$

where

$$Q_{\pm} = A^2 \epsilon_0 - iB^2 (\epsilon_0 \pm \epsilon_{11}).$$

The alternative approach we presented in Eqs. (13)–(16) provides identical solutions, where the half-space scattering coefficients read

$$\begin{aligned} \bar{r}_{FT}^{(1)} &= \frac{iA^2 \epsilon_0 - B^2 (\epsilon_0 + \epsilon_{11})}{Q_+}, \\ \bar{r}_V^{(1)} &= \frac{iQ_-}{Q_+}, \quad \bar{r}_V^{(2)} = \frac{-iQ_-}{Q_+}, \\ \bar{t}_V^{(1)} &= \bar{t}_{FT}^{(1)} = \bar{t}_{FT}^{(2)} = \frac{2iAB\sqrt{i\epsilon_0 \epsilon_{11}}}{Q_+}, \end{aligned}$$

and the multiple reflection factor is

$$f_m(d) = \frac{Q_+^2 e^{k_x d}}{Q_+^2 e^{2k_x d} - Q_-^2}. \quad (20)$$

Figure 3(a) shows plots of the magnitudes of the tunneling transmission coefficients $|t_{FT}|$ of the fast transverse SH wave [calculated from Eq. (19)] across a vacuum gap structure separating ZnO crystals with $6mm$ hexagonal symmetry oriented as in Fig. 2(a), as a function of the incident angle θ_i , with three different scaled vacuum gap values kd , where k is the magnitude of the incident wave vector. The ZnO material constants adopted in the calculation are $\rho = 5680 \text{ kg m}^{-3}$, $c_{44} = 4.247 \times 10^{10} \text{ N m}^{-2}$, $e_{15} = -0.48 \text{ C m}^{-2}$, and $\epsilon_{11} = 8.55\epsilon_0$ [3]. The main observation is that transmission remains modest, except at small glancing angles (near 90° incidence), where a maximum can be found at θ_0 . For small enough gaps with $kd < 1$, this transmission peak approaches unity. The peak transmission condition can be found by setting the real part of the denominator in Eq. (19) to zero, giving an equation for θ_0 :

$$B^4 \equiv \frac{(A^2 + c_{44}/\epsilon_{11})^2}{\tan^2 \theta_0} = \frac{A^4 \epsilon_0^2 (e^{2k_x d} - 1)}{(\epsilon_0 + \epsilon_{11})^2 e^{2k_x d} - (\epsilon_0 - \epsilon_{11})^2}. \quad (21)$$

Furthermore, when the gap size approaches zero, the transmission coefficient, Eq. (19), is simplified to the expression $t_{FT} = A^2/(A^2 - iB^2)$, which approaches unity when $\theta \rightarrow 90^\circ$. Conversely, our expressions demonstrate that the transmission is never mathematically exactly one for a finite gap size.

Similar analytical results for an incoming SH mode for the same crystal orientations have also been demonstrated for LiIO_3 (hexagonal class 6 symmetry) and $\text{Bi}_{12}\text{GeO}_{20}$ (cubic class 23 symmetry) by Balakirev and Gorchakov [13], who attributed the peak transmission to phase matching of the incident and transmitted waves. They did not, however, give

explicit formulas for $6mm$ symmetry. For the lower class 6 symmetry of their study, they showed that a range of angles can be found for complete transmission with a finite small gap size, in contrast with our findings for the $6mm$ -symmetry case.

Figure 3(b) gives a closer look of the angle of maximum transmission θ_0 and its corresponding peak transmission value. The range of angles that can satisfy the condition is tightly limited to lie within a range of 0.4 degrees, and with an increasing gap size beyond the characteristic length $kd \approx 1$, the peak transmission quickly drops to zero. The dependence of the transmission coefficient on the gap size is more clearly presented in Fig. 3(c). The bulk acoustic wave tunneling is switched off at about $kd \geq 1$, whereas the transmission is saturated for gap sizes smaller than about $kd \leq 10^{-2}$. The smallest incident angles providing a transmission factor larger than 10% are around $\approx 60^\circ$ for small gaps.

B. Numerical results for arbitrarily oriented hexagonal ZnO crystals

The reflection and transmission coefficients of arbitrarily oriented crystals can also be obtained numerically by following our theoretical approach. Here, we demonstrate two sets of results (two cuts) for hexagonal $6mm$ ZnO crystals that been cut into two pieces and separated by a vacuum gap of distance d . In other words, we only consider here that the two crystals have the same orientation.

Due to the uniaxial symmetry, the orientation of the crystals can be fixed by just two angles: the crystal zenith angle ϑ and the crystal azimuth angle φ [see Fig. 7(b)]. The details of the definition of the crystal orientation, the rotation procedure and the transformations of the material tensors are described in Appendix F. Both semi-infinite bulk crystals share this identical crystal orientation in which the zenith angle ϑ is fully determined by the plane of the cut (see Appendix H for the common cut planes for a hexagonal crystal), whereas the rotation of the crystal azimuth angle φ is equivalent to the rotational degree of freedom of the incident wave (the orientation of the sagittal plane) around the normal of the interface plane. The incident wave has two degrees of freedom: One is the incident angle θ_i that resides inside the sagittal plane and varies from 0° to 90° . The other is the incident azimuth angle that varies from 0° to 360° . For the cases demonstrated in this section, the rotation of the crystal azimuth angle φ can be considered either as a change of the incident wave azimuth angle, or a change of the crystal orientation. In the computations here, we implemented it as a rotation of the crystal, to avoid duplication.

The numerical algorithms were implemented by using the Anaconda Python distribution. Here, we briefly explain the workflow of the implementation of the combined boundary condition approach presented in Sec. III A. A set of input parameters specifying the material constants (tensors ϵ_0^S , e_0 , c_0^E , and scalar ρ , values from Ref. [3]), the crystal orientation (ϑ , φ), the gap distance d , and the incident angle θ_i and the mode of the incident bulk wave are first given. With the material constants and crystal orientation, the rotated material parameters (ϵ^S , e , c^E) can be obtained by using the formulation described in Appendix F.

Knowing the rotated material parameters and the incident angle and mode, the parallel component of the incident wave phase velocity v_x is solved from the piezoelectrically stiffened Christoffel equations (for details, see standard textbooks, e.g., Refs. [2,3]). By combining the rotated material constants and the phase velocity v_x , the 8×8 Stroh matrix $N(v_x)$ given by Eq. (B9) can be constructed, whose eigenvalues p_α and eigenvectors ξ_α are then solved from Eq. (3). The orthogonality of the eigenvectors are then checked and they are normalized using the Stroh-normalization condition, Eq. (4).

At this point, we can begin to solve the boundary-condition problem of Eq. (9). By following our first approach, two 8×5 vacuum matrices M_1 and M_2 can be constructed from Eq. (10) based on d and v_x ; the 8×8 matrix M can be formed by combining the vacuum matrices and the eigenvector solutions of the Stroh matrix; and the column vector $U_{in}^{(1)}$ can be constructed from the incident mode eigenvector ξ_{in} . Finally, with these computed matrices, the transmission and reflection coefficients of the incident bulk electroacoustic wave can be acquired from Eq. (12). The computational time of each of the above processes took less than 1 ms, with an overall time less than 5 ms using a standard modern laptop. A set of results with a two varying incident angles, as shown in Figs. 4 and 5 then took 6 minutes each.

In the first set of results, shown in Fig. 4, we start from an a -plane-cut crystal with $\varphi = 0^\circ$, which describes an orientation that is identical to the analytical example in Sec. IV A. Then, we gradually rotate the crystal orientation around the z axis, the normal of the interfaces, from $\varphi = 0^\circ \rightarrow 360^\circ$ [see Fig. 2(b)].

We have chosen to plot just the most interesting example cases in Fig. 4, as our goal here is to demonstrate the capabilities of the formalism. We plot the magnitudes of tunneling amplitude transmission coefficients $|t_\alpha|$ of incident fast transverse (FT) and slow transverse (ST) wave modes, and their mode converted transmission amplitudes (i.e., FT \rightarrow FT, FT \rightarrow ST, ST \rightarrow ST, ST \rightarrow FT), as a function of the incident angle θ_i and the rotation angle φ , keeping the scaled gap $kd = 10^{-2}$ constant. (The mode assignment process is discussed in Appendix G). In comparison with the FT and ST modes, the transmission of the L mode is much weaker, does not show as many interesting features, and we choose not to use it as an example here. In addition, we plot the critical incident angles, beyond which a faster reflected partial-wave mode becomes evanescent. Thus, for the incident FT mode, only one critical angle exists, where the L mode becomes evanescent (θ_{L_c}), whereas for the incident ST mode, there are two critical angles: for the L mode θ_{L_c} and for the FT mode θ_{FT_c} .

Since for this first crystal orientation example the azimuthal rotation axis φ is perpendicular to the crystal uniaxial c axis, we expect and observe a mirrored twofold symmetry in the plots. With an incident FT mode, several isolated high transmission areas are observed, and they are primarily located at small glancing angles (large θ_i) around high-symmetry orientations. In particular, the line segment of $\varphi = 0^\circ$ and $\theta_i \in [0^\circ, 90^\circ]$ for FT \rightarrow FT represents the same results as already discussed in the analytical calculation in Sec. IV A. However, with crystal orientations around $\varphi = 90^\circ$ and 270° , the high transmission region lies just after the critical angle θ_{L_c} . Another general observation is that for both modes, the

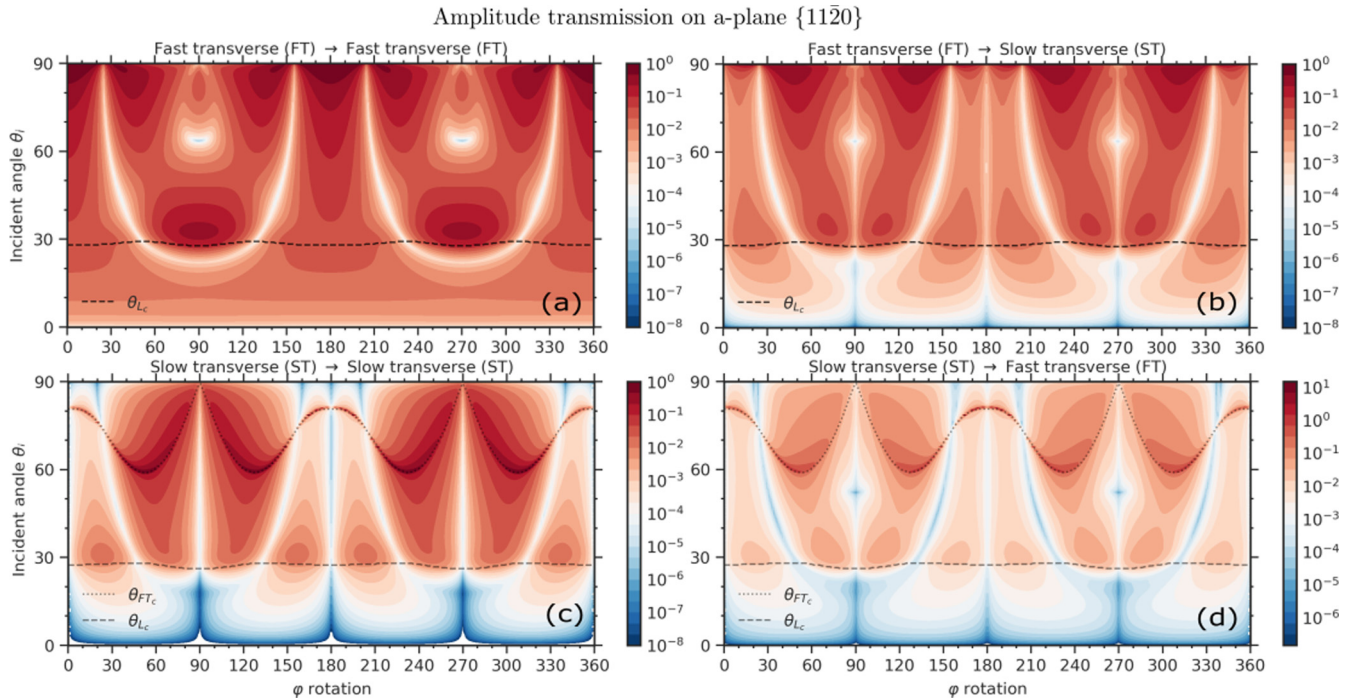


FIG. 4. The magnitudes of amplitude transmission coefficients $|t_\alpha|$ across a vacuum gap (color scale) of an a -plane-cut ZnO crystal ($11\bar{2}0$) versus incident angle θ_i and z axis rotation angle φ for a scaled gap $kd = 10^{-2}$. Two different incident wave modes (FT, ST) and two transmitted wave modes (FT, ST) are demonstrated: (a) FT-to-FT, (b) FT-to-ST, (c) ST-to-ST, and (d) ST-to-FT transmission. θ_{L_c} (dashed) and θ_{FT_c} (dotted) are the critical angles for scattered L and FT wave modes. Note that panel (d) has a different logarithmic scale, as in the mode conversion $|t_\alpha| > 1$ is possible.

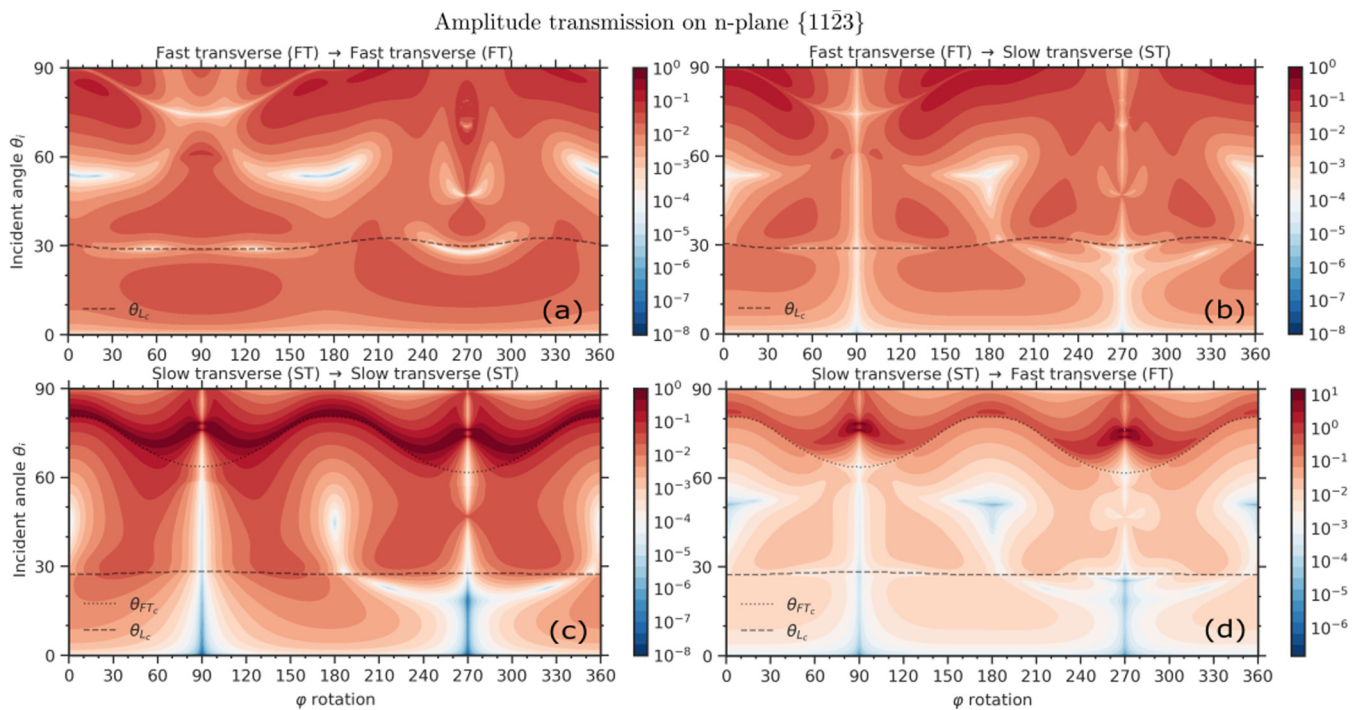


FIG. 5. The magnitudes of amplitude transmission coefficients $|t_\alpha|$ across a vacuum gap (color scale) of an n -plane-cut ZnO crystal ($11\bar{2}3$) versus incident angle θ_i and z -axis rotation angle φ , for a scaled gap $kd = 10^{-2}$. Two different incident wave modes (FT, ST) and two transmitted wave modes (FT, ST) are demonstrated: (a) FT-to-FT, (b) FT-to-ST, (c) ST-to-ST, and (d) ST-to-FT transmission. θ_{L_c} (dashed) and θ_{FT_c} (dotted) are the critical angles for scattered L and FT wave modes. Note that panel (d) has a different logarithmic scale, as in the mode conversion $|t_\alpha| > 1$ is possible.

transmission is significantly enhanced when θ_i is beyond θ_{L_c} , as more energy is then concentrated near the interfaces.

With an incident ST mode, in contrast, a narrow high transmission “resonance” exists close to the critical angle of the FT partial waves (θ_{FT_c}) in the first intersonic interval, and is significantly enhanced around $\varphi = n\pi/3$, $n = 1, 2, \dots$. Such a resonant transmission could be interpreted as arising from the excitation of leaky surface wave modes coupling across the gap [31]. In addition to resonant features, “antiresonances,” or sharp dips, can also be observed in the transmission. In particular the u-shaped feature between $\varphi \approx 20^\circ \dots 160^\circ$ and $\varphi \approx 200^\circ \dots 340^\circ$ is prominent in all plots.

In the second crystal cut example of Fig. 5, we demonstrate the same FT and ST mode results for ZnO, but which is now initially cut from a crystallographic plane of $\{11\bar{2}3\}$ [n plane, see Fig. 2(c) and Appendix H for common cut planes for a hexagonal crystal]. The change in the crystal orientation dramatically distorts the amplitude transmission as a function of both θ_i and φ . The twofold symmetry with respect to φ rotations is lost, and with an incident FT mode, the transmission is generally attenuated compared with the a -plane results. To understand this, we consider for example the case $\varphi = 0$ in the n -plane crystal cut, for which the incident FT mode is a quasitransverse mode which now couples to all other acoustic modes at the interface. As a result, the FT \rightarrow FT transmission is attenuated, while the mode converted FT \rightarrow ST transmission increases. In contrast, with the a -plane cut the incident FT mode wave is a pure horizontal shear wave (SH), as described in the analytical example, leading intuitively to a stronger FT \rightarrow FT transmission and vanishing FT \rightarrow ST transmission. Furthermore, it is interesting to see that, with an incident ST mode, significant transmission resonance just beyond the FT wave critical angle θ_{FT_c} still survives as a robust feature also for the n cut. As mentioned above, this can be interpreted as excitation of coupled leaky surface waves between the vacuum interfaces [31].

V. CONCLUSIONS AND OUTLOOK

We have shown that in general, bulk acoustic waves can be transmitted (“tunnel”) across a finite vacuum gap between two piezoelectric crystals. This mechanism works not only in the nanoscale, but also for large gap widths of the order of the wavelength. Here, we presented a rigorous general approach and formalism that can be applied to study this effect for any anisotropic piezoelectric crystals with arbitrary crystallographic orientation, acquiring the solutions of reflection and transmission coefficients of all the partial waves. The extended Stroh formalism, briefly reviewed for the benefit of the reader, was used as a powerful tool to solve in general the scattering of an electroacoustic wave on the solid-vacuum interface. Two new approaches to solve the reflection and transmission coefficients of the coupled tunneling problem (two interfaces separated by a gap) were then derived: one based on the direct solution of the boundary conditions, the other on the physical picture of multiple reflections of evanescent waves in the vacuum gap. In particular, the multiple reflection method provides a physical insight of the acoustic tunneling that is analogous to near-field tunneling of evanescent electromagnetic waves. In this picture, the effect of the

vacuum gap size on the reflection and transmission coefficients is conveniently separated and described by a single multiple reflection factor, offering a potential computational advantage.

To verify the usefulness and validity of the methodology, explicit example solutions for the case of two adjacent ZnO wurtzite hexagonal crystals were demonstrated. First, we presented analytical results for a fast transverse incident mode and high-symmetry crystal orientation. Simple expressions for the transmission and reflection coefficients and the multiple reflection factor were derived, and an explicit mathematical condition for the peak transmission was also presented. We made the observation that tunneling transmission is not necessarily small: For small glancing angle incidence, transmission was approaching one for gap sizes smaller than the wavelength.

Second, we described the workflow for numerical implementation for an arbitrary orientation and presented some numerical results for two cases of anisotropic ZnO crystals (two different crystal cut surfaces). We plotted the transmission coefficients of the fast and slow transverse partial modes, as well as the conversion between them, against the incident angle and the crystal azimuth rotation angle. In the numerical examples, we also find close to unity transmissions, and not only for small glancing angles. Such cases were mostly observed in the vicinity of the critical angles of the scattered partial-wave modes, where they become inhomogeneous surface modes. The enhancement of tunneling transmission was a particularly sharp and strong feature (resonance) for an incoming slow transverse wave with an incident angle just beyond the critical angle for the fast transverse wave, where coupled leaky surface waves can be excited.

With the formalism and the approaches derived in this work, we have set the foundation for many further studies of electroacoustic wave tunneling. The first straightforward objective is to map and understand the conditions for exceptionally high transmission, as there are indications of the possibility of complete acoustic wave tunneling. In addition to direct applications in the manipulation of acoustic waves, our formalism can be applied in the future in other areas of physics related to vibrations, such as heat transport, optomechanics, and quantum information science.

ACKNOWLEDGMENTS

This study was supported by the Academy of Finland Project No. 341823. We wish to acknowledge discussions with Dr. Tuomas Puurtinen.

APPENDIX A: PLANE-WAVE EQUATIONS OF MOTION AND CONSTITUTIVE EQUATIONS IN QUASISTATIC APPROXIMATION

Here we clarify the definitions of the variables in Eqs. (1), presented in the abbreviated (Voigt) matrix notation. The first equation in the set, the acoustic field equation, reads in general (if no external body forces are present)

$$\nabla \cdot \sigma = \rho \frac{\partial^2 \mathbf{u}}{\partial t^2},$$

where σ is the stress tensor and \mathbf{u} is the displacement vector. Transforming it into the abbreviated Voigt notation, where the capital Voigt index K runs over six coordinate pairs $K = xx, yy, zz, yz, xz, xy$, will result in a matrix equation $\nabla_{iK}\sigma_K = \rho \frac{\partial^2 u_i}{\partial t^2}$ where the index i denotes the usual Cartesian component and repeated indices are summed. Thus, ∇_{iK} defines a 3×6 differential operator matrix [see, for example, Ref. [3] Eq. (2.36) for an explicit expression]. For harmonic plane waves, such an operator is replaced by a 3×6 matrix formed by the wave-vector components $-ik_{iK}$, explicitly defined as [3]

$$\hat{\mathbf{k}} = \begin{bmatrix} k_x & 0 & 0 & 0 & k_z & k_y \\ 0 & k_y & 0 & k_z & 0 & k_x \\ 0 & 0 & k_z & k_y & k_x & 0 \end{bmatrix}, \quad (\text{A1})$$

and the second derivative w.r.t time is replaced by $-\omega^2$, yielding the first equation in Eq. (1) in the main text,

$$ik_{iK}\sigma_K = \rho\omega^2 u_i. \quad (\text{A2})$$

The second equation, Gauss's law $\nabla \cdot \mathbf{D} = 0$, is the only Maxwell's equation that needs to be satisfied within the quasistatic approximation. It contains the usual vector divergence operator, and it can directly be written in the component form as $\nabla_i D_i = 0$, which gives for the plane waves the equation in the main text,

$$-ik_i D_i = 0, \quad (\text{A3})$$

where k_i are now simply the Cartesian components of the wave vector.

The third and the fourth equations in Eqs. (1) are the constitutive relations for piezoelectrics, coupling the elastic and electric variables. They are given in abbreviated notation for the stress as $\sigma_K = c_{KL}^E s_L - e_{Kj} E_j$ and for the electric displacement $D_i = \epsilon_{ij}^S E_j + e_{iL} s_L$, where s_L is the strain tensor, E_i is the electric field, and c_{KL}^E , e_{Kj} , and ϵ_{ij}^S are the material parameters: the elastic stiffness tensor at constant electric field, the piezoelectric strain tensor, and the electric permittivity tensor at constant strain, respectively. The constitutive relations simplify in the quasistatic case by writing them in terms of the displacement u_i and the electric potential Φ , $s_L = \nabla_{Lj} u_j$, $E_i = -\nabla_i \Phi$, and as before for the plane waves the differential operators can be substituted by $\nabla_{Lj} \rightarrow -ik_{Lj}$, $\nabla_i \rightarrow -ik_i$, which lead to the forms presented in Eqs. (1):

$$\begin{aligned} \sigma_K &= -ic_{KL}^E k_{Lj} u_j - ie_{Kj} k_j \Phi, \\ D_i &= -ie_{iL} k_{Lj} u_j + i\epsilon_{ij}^S k_j \Phi. \end{aligned} \quad (\text{A4})$$

APPENDIX B: EXTENDED STROH FORMALISM

In this Appendix, we provide the derivation for the piezoelectric Stroh eigenequation, Eq. (3), in the quasistatic approximation, including all necessary definitions, and provide a few remarks about the normalization. Under the framework of the quasistatic approximation, one can derive the normal projections of the stress and electric displacement fields using the piezoelectric constitutive equations in Eq. (1)

as

$$\begin{aligned} \mathbf{n} \cdot \boldsymbol{\sigma} &= -in_{iK} c_{KL}^E k_{Lj} u_j - in_{iK} e_{Kj} k_j \Phi, \\ \mathbf{n} \cdot \mathbf{D} &= -in_i e_{iL} k_{Lj} u_j + in_i \epsilon_{ij}^S k_j \Phi, \end{aligned} \quad (\text{B1})$$

where n_i is the i th Cartesian component of the inward unit normal vector \mathbf{n} of the piezo-vacuum surface, and the 3×6 matrix n_{iK} has the same structure as k_{iK} , but is now formed by the unit normal components n_i , explicitly written as

$$\hat{\mathbf{n}} = \begin{bmatrix} n_x & 0 & 0 & 0 & n_z & n_y \\ 0 & n_y & 0 & n_z & 0 & n_x \\ 0 & 0 & n_z & n_y & n_x & 0 \end{bmatrix}. \quad (\text{B2})$$

If we introduce a matrix expression (\mathbf{nk}) for a 4×4 matrix that is defined as

$$(\mathbf{nk}) \equiv \begin{bmatrix} n_{iK} & 0 \\ 0 & n_i \end{bmatrix} \begin{bmatrix} c_{KL}^E & e_{Kj} \\ e_{iL} & -\epsilon_{ij}^S \end{bmatrix} \begin{bmatrix} k_{Lj} & 0 \\ 0 & k_j \end{bmatrix}, \quad (\text{B3})$$

where the elements of the matrices represent submatrices instead of scalars (n_{iK} represents the matrix $\hat{\mathbf{n}}$, etc.), it is straightforward to show that Eqs. (B1) can be written in the following more compact notation:

$$\begin{bmatrix} \mathbf{n} \cdot \boldsymbol{\sigma} \\ \mathbf{n} \cdot \mathbf{D} \end{bmatrix} = -i(\mathbf{nk}) \begin{bmatrix} \mathbf{u} \\ \Phi \end{bmatrix}. \quad (\text{B4})$$

By adopting the general field solutions for a mode α in Eqs. (2) and decomposing the k vector $\mathbf{k} = k_x(\mathbf{m} + p_\alpha \mathbf{n})$ using the two orthogonal unit vectors \mathbf{m} and \mathbf{n} , where \mathbf{m} is parallel to the piezo-vacuum interfaces, we can further arrange Eq. (B4) into a form where the unknown p_α is separated into the right-hand side of the equation:

$$-(\mathbf{nn})^{-1}(\mathbf{nm}) \begin{bmatrix} \mathbf{A}_\alpha \\ \phi_\alpha \end{bmatrix} - (\mathbf{nn})^{-1} \begin{bmatrix} \mathbf{L}_\alpha \\ \mathbf{D}_\alpha^n \end{bmatrix} = p_\alpha \begin{bmatrix} \mathbf{A}_\alpha \\ \phi_\alpha \end{bmatrix}. \quad (\text{B5})$$

The matrices (\mathbf{nn}) and (\mathbf{nm}) are defined analogously to Eq. (B3) and thus depend only on the material parameters and the orientation of the crystal. We note that real materials do not present any pathological cases where the matrix inverse $(\mathbf{nn})^{-1}$ would not exist.

Furthermore, the equation of motion and Gauss's law can also be organized into a similar linear equations set:

$$(\mathbf{kk}) \begin{bmatrix} \mathbf{u} \\ \Phi \end{bmatrix} = \rho\omega^2 \mathbf{I}' \begin{bmatrix} \mathbf{u} \\ \Phi \end{bmatrix}, \quad (\text{B6})$$

in which \mathbf{I}' is a 4×4 matrix with elements $I'_{ii} = 1$, $i = 1, 2, 3$ and others zero.

By decomposing the k vector as above and substituting the expression for $p_\alpha [\mathbf{A}_\alpha, \phi_\alpha]^T$ from Eq. (B5), we obtain

$$\begin{aligned} & - [(\mathbf{mn})(\mathbf{nn})^{-1}(\mathbf{nm}) - (\mathbf{mm}) + \rho v_x^2 \mathbf{I}'] \begin{bmatrix} \mathbf{A}_\alpha \\ \phi_\alpha \end{bmatrix} \\ & - (\mathbf{mn})(\mathbf{nn})^{-1} \begin{bmatrix} \mathbf{L}_\alpha \\ \mathbf{D}_\alpha^n \end{bmatrix} = p_\alpha \begin{bmatrix} \mathbf{L}_\alpha \\ \mathbf{D}_\alpha^n \end{bmatrix}, \end{aligned} \quad (\text{B7})$$

where $v_x = \omega/k_x$. Finally, combining Eqs. (B5) and (B7) by defining an eight-dimensional eigenvector $\boldsymbol{\xi}_\alpha = [\mathbf{A}_\alpha, \phi_\alpha, \mathbf{L}_\alpha, \mathbf{D}_\alpha^n]^T$, we have derived the eigenequation for the piezoelectric scattering problem, Eq. (3):

$$N(v_x)\boldsymbol{\xi}_\alpha = p_\alpha \boldsymbol{\xi}_\alpha, \quad (\text{B8})$$

where the 8×8 real matrix N reads

$$N(v_x) = - \begin{bmatrix} (nn)^{-1}(nm) & (nn)^{-1} \\ (mn)(nn)^{-1}(nm) - (mm) + \rho v_x^2 I' & (mn)(nn)^{-1} \end{bmatrix}. \tag{B9}$$

The set of eigenvectors ξ_α are orthogonal and form a complete set in the usual case, where the eigenvalues p_α are distinct [16]. In a few isolated situations, nonsemisimple degeneracy can occur, in which case generalized eigenvectors can be introduced [18,28]. We do not consider those special cases (transonic states) in this study because numerically one can always solve the problem in a limiting manner very close to such a special point.

In the main text, we quoted the orthonormalization condition in Eq. (4). It follows [18,19] from the symmetry condition for the auxiliary matrix $\hat{T}N$

$$(\hat{T}N)^T = \hat{T}N,$$

where

$$\hat{T} = \begin{bmatrix} \hat{O}_{(4)} & \hat{I}_{(4)} \\ \hat{I}_{(4)} & \hat{O}_{(4)} \end{bmatrix}, \tag{B10}$$

with which a reciprocal eigenvector set $T\xi_\alpha$ orthogonal to ξ_α can be defined. It follows that the eigenvectors satisfy the relation

$$\xi_\alpha \cdot \hat{T}\xi_\beta = \xi_\alpha^T \hat{T}\xi_\beta = \delta_{\alpha\beta}, \quad \alpha, \beta = 1, \dots, 8, \tag{B11}$$

where $\delta_{\alpha\beta}$ is the Kronecker delta. We stress here that the dot symbol has the meaning of a matrix product in this context, as exemplified by the second form. In particular, it does not denote a complex inner product, in which case complex conjugation would be included for one of the vectors.

Equation (B11) [identical to Eq. (4) in the main text] is thus readily available as the orthonormalization condition to secure a unique normalized eigenvector solution for the N matrix. In addition, the orthonormalization condition Eq. (B11) leads to a completeness condition

$$\sum_\alpha \xi_\alpha \otimes \hat{T}\xi_\alpha = \hat{I}_{(8)}, \tag{B12}$$

providing us a powerful tool to ensure the accuracy of the solutions.

APPENDIX C: MATRIX SOLUTION OF THE BOUNDARY CONDITIONS

In this Appendix, to avoid cumbersome expressions $D_\alpha^{n,(i)}$ and $D_{V_\pm}^n$ with the explicit superscript n , we will use the shorthand notation $D_\alpha^{(i)}$ and D_{V_\pm} in their place to represent the Stroh eigenvector components for the normal projection of the electric displacement in Eq. (2) in the solid $i = 1, 2$ and in vacuum (V), respectively.

The boundary conditions of the tunneling problem, Eqs. (9), provide a total of ten linear equations corresponding to ten partial-wave amplitude solutions $(b_1^{(1)}, \dots, b_4^{(1)}, \tilde{b}_1^{(2)}, \dots, \tilde{b}_4^{(2)}, b_{V\pm})$. Here, we list explicitly

all the boundary conditions included in Eqs. (9):

$$\begin{aligned} b_{in}^{(1)}\phi_{in}^{(1)} + \sum_{\alpha=1}^4 b_\alpha^{(1)}\phi_\alpha^{(1)} &= b_{V+}\phi_{V+} + b_{V-}\phi_{V-}, \\ b_{in}^{(1)}D_{in}^{(1)} + \sum_{\alpha=1}^4 b_\alpha^{(1)}D_\alpha^{(1)} &= b_{V+}D_{V+} + b_{V-}D_{V-}, \\ b_{in}^{(1)}L_{in}^{(1)} + \sum_{\alpha=1}^4 b_\alpha^{(1)}L_\alpha^{(1)} &= \hat{O}_{(3)}, \\ \sum_{\alpha=1}^4 \tilde{b}_\alpha^{(2)}\phi_\alpha^{(2)} &= b_{V+}\phi_{V+}e^{-k_x d} + b_{V-}\phi_{V-}e^{k_x d}, \\ \sum_{\alpha=1}^4 \tilde{b}_\alpha^{(2)}D_\alpha^{(2)} &= b_{V+}D_{V+}e^{-k_x d} + b_{V-}D_{V-}e^{k_x d}, \\ \sum_{\alpha=1}^4 \tilde{b}_\alpha^{(2)}L_\alpha^{(2)} &= \hat{O}_{(3)}. \end{aligned} \tag{C1}$$

The goal of this Appendix is to rearrange the above boundary conditions into a simple matrix equation that separates the incident wave properties, the information about the materials properties and the vacuum gap, and the scattered amplitudes, i.e., by writing

$$\hat{y} = M\hat{x}, \tag{C2}$$

where \hat{y} is a 8×1 column vector that contains the information about the incident wave and M is a 8×8 matrix, both to be derived below, and \hat{x} is a 8×1 column vector containing the wave amplitudes of all scattered waves (and therefore the information on the transmission and reflection coefficients):

$$\hat{x} = [b_1^{(1)}, \dots, b_4^{(1)}, \tilde{b}_1^{(2)}, \dots, \tilde{b}_4^{(2)}]^T.$$

By eliminating $b_{V\pm}$ from Eq. (C1), the number of linear equations provided by the boundary conditions in Eq. (C1) can be reduced from ten to eight:

$$\begin{aligned} V_1^{-1} \left(\begin{bmatrix} \phi_{in}^{(1)} \\ D_{in}^{(1)} \end{bmatrix} b_{in}^{(1)} + \sum_{\alpha=1}^4 \begin{bmatrix} \phi_\alpha^{(1)} \\ D_\alpha^{(1)} \end{bmatrix} b_\alpha^{(1)} \right) &= V_2^{-1} \left(\sum_{\alpha=1}^4 \begin{bmatrix} \phi_\alpha^{(2)} \\ D_\alpha^{(2)} \end{bmatrix} \tilde{b}_\alpha^{(2)} \right), \\ b_{in}^{(1)}L_{in}^{(1)} + \sum_{\alpha=1}^4 b_\alpha^{(1)}L_\alpha^{(1)} &= \hat{O}_{(3)}, \\ \sum_{\alpha=1}^4 \tilde{b}_\alpha^{(2)}L_\alpha^{(2)} &= \hat{O}_{(3)}, \end{aligned} \tag{C3}$$

where

$$V_1 = \begin{bmatrix} \phi_{V+} & \phi_{V-} \\ D_{V+} & D_{V-} \end{bmatrix}, \quad V_2 = \begin{bmatrix} \phi_{V+}e^{-k_x d} & \phi_{V-}e^{k_x d} \\ D_{V+}e^{-k_x d} & D_{V-}e^{k_x d} \end{bmatrix}.$$

The 2×2 matrices V_1 and V_2 are not dependent on the incoming or scattered wave properties except for the conserved wave-vector component k_x .

To combine all equations in Eqs. (C3) into one matrix equation, we can move all the terms depending on $b_{in}^{(1)}$ to the

right and all the others to the left and write all equations in terms of 5×1 column vectors $U_\gamma^{(i)} = [\phi_\gamma^{(i)}, D_\gamma^{(i)}, L_\gamma^{(i)}]^T$ containing the reflected ($U_\alpha^{(1)}$), transmitted ($U_\alpha^{(2)}$) and input wave ($U_{in}^{(1)}$) Stroh eigenvector components for the electric potential, electric displacement and traction force. This way we obtain

$$\begin{aligned} \sum_{\alpha=1}^4 ([V_1^{-1} \quad \hat{\mathbf{O}}_{(2 \times 3)}] U_\alpha^{(1)} b_\alpha^{(1)} - [V_2^{-1} \quad \hat{\mathbf{O}}_{(2 \times 3)}] U_\alpha^{(1)} \tilde{b}_\alpha^{(2)}) &= -[V_1^{-1} \quad \hat{\mathbf{O}}_{(2 \times 3)}] U_{in}^{(1)} b_{in}^{(1)}, \\ \sum_{\alpha=1}^4 ([\hat{\mathbf{O}}_{3 \times 2} \quad \hat{\mathbf{I}}_{(3)}] U_\alpha^{(1)} b_\alpha^{(1)} - [\hat{\mathbf{O}}_{3 \times 2} \quad \hat{\mathbf{O}}_{(3 \times 3)}] U_\alpha^{(2)} \tilde{b}_\alpha^{(2)}) &= -[\hat{\mathbf{O}}_{3 \times 2} \quad \hat{\mathbf{I}}_{(3)}] U_{in}^{(1)} b_{in}^{(1)}, \\ \sum_{\alpha=1}^4 ([\hat{\mathbf{O}}_{3 \times 2} \quad \hat{\mathbf{O}}_{(3 \times 3)}] U_\alpha^{(1)} b_\alpha^{(1)} - [\hat{\mathbf{O}}_{3 \times 2} \quad \hat{\mathbf{I}}_{(3)}] U_\alpha^{(2)} \tilde{b}_\alpha^{(2)}) &= -[\hat{\mathbf{O}}_{3 \times 2} \quad \hat{\mathbf{O}}_{(3 \times 3)}] U_{in}^{(1)} b_{in}^{(1)}, \end{aligned} \quad (C4)$$

where $\hat{\mathbf{O}}_{n \times m}$ denotes a zero matrix of dimensions $n \times m$, and $\hat{\mathbf{I}}_{(3)}$ is the 3×3 identity matrix.

From the above form, Eqs. (C4), we see that a single matrix equation

$$\sum_{\alpha=1}^4 (M_1 U_\alpha^{(1)} b_\alpha^{(1)} - M_2 U_\alpha^{(2)} \tilde{b}_\alpha^{(2)}) = -M_1 U_{in}^{(1)} b_{in}^{(1)} \quad (C5)$$

can be written if we define the 8×5 matrices M_1 and M_2 as

$$M_1 = \begin{bmatrix} V_1^{-1} & \hat{\mathbf{O}}_{(2 \times 3)} \\ \hat{\mathbf{O}}_{(3 \times 2)} & \hat{\mathbf{I}}_{(3)} \\ \hat{\mathbf{O}}_{(3 \times 2)} & \hat{\mathbf{O}}_{(3 \times 3)} \end{bmatrix}, \quad M_2 = \begin{bmatrix} V_2^{-1} & \hat{\mathbf{O}}_{(2 \times 3)} \\ \hat{\mathbf{O}}_{(3 \times 2)} & \hat{\mathbf{O}}_{(3 \times 3)} \\ \hat{\mathbf{O}}_{(3 \times 2)} & \hat{\mathbf{I}}_{(3)} \end{bmatrix}. \quad (C6)$$

Finally, by comparing Eq. (C5) with the targeted expression $\hat{y} = M \hat{x}$ [Eq. (C2), remembering that $\hat{x} = [b_1^{(1)}, \dots, b_4^{(1)}, \tilde{b}_1^{(2)}, \dots, \tilde{b}_4^{(2)}]^T$], we obtain $\hat{y} = -M_1 U_{in} b_{in}$, with the 8×8 matrix M formed by combining eight 8×1 column matrix blocks as

$$M = [M_1 U_1^{(1)}, M_1 U_2^{(1)}, M_1 U_3^{(1)}, M_1 U_4^{(1)}, \\ -M_2 U_1^{(2)}, -M_2 U_2^{(2)}, -M_2 U_3^{(2)}, -M_2 U_4^{(2)}],$$

which is the definition given in the main text in Eq. (11). From the above, we see that, in the matrix M , the submatrices M_1 and M_2 depend only on the vacuum permittivity ϵ_0 ($D_{V_\pm} = \pm i \epsilon_0 \phi_{V_\pm}$ and $\phi_{V_\pm} = 1/\sqrt{\pm 2i \epsilon_0}$, Sec. III in the main text), the gap distance d and the conserved incident wave k -vector component k_x ; vectors U_γ are the physical solutions obtained from the eigenvectors ξ_γ in the extended Stroh formalism.

Finally, the four reflection and four transmission coefficients of the wave amplitudes can readily be obtained as

$$\begin{bmatrix} \mathbf{r}_{(4 \times 1)} \\ \mathbf{t}_{(4 \times 1)} \end{bmatrix} = \frac{\hat{x}}{b_{in}} = -M^{-1} M_1 U_{in}. \quad (C7)$$

APPENDIX D: SCATTERING MATRIX

If we consider a scattering problem for an interface i between a piezoelectric crystal and vacuum, as illustrated in Fig. 6, the scattering matrix $S^{(i)}$ determining how input waves

scatter into output waves can be defined as

$$\begin{bmatrix} b_1^{(i)} \\ b_2^{(i)} \\ b_3^{(i)} \\ b_4^{(i)} \\ b_t^{(V)} \end{bmatrix} = S^{(i)} \begin{bmatrix} b_{in}^{(i)} \\ b_{in}^{(V)} \end{bmatrix} = \begin{bmatrix} \bar{r}_1^{(i)} & \bar{t}_1^{(i)} \\ \bar{r}_2^{(i)} & \bar{t}_2^{(i)} \\ \bar{r}_3^{(i)} & \bar{t}_3^{(i)} \\ \bar{r}_4^{(i)} & \bar{t}_4^{(i)} \\ \bar{t}_{in}^{(i)} & \bar{r}_{in}^{(i)} \end{bmatrix} \begin{bmatrix} b_{in}^{(i)} \\ b_{in}^{(V)} \end{bmatrix}, \quad (D1)$$

where the superscript (V) denotes the evanescent electric potential wave in the vacuum gap.

The first boundary condition in Eq. (9) can then be rearranged by moving all the outgoing (incoming) waves to the left (right) side, giving

$$[U_1^{(1)}, U_2^{(1)}, U_3^{(1)}, U_4^{(1)}, -U_{V_+}] \begin{bmatrix} b_1^{(1)} \\ b_2^{(1)} \\ b_3^{(1)} \\ b_4^{(1)} \\ b_{V_+} \end{bmatrix} = [-U_{in}^{(1)}, U_{V_-}] \begin{bmatrix} b_{in}^{(1)} \\ b_{V_-} \end{bmatrix}. \quad (D2)$$

The second boundary condition follows from Eq. (D2) by changing the medium index, and exchanging the incoming

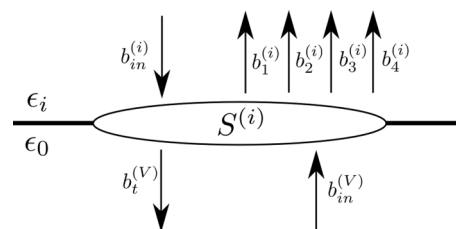


FIG. 6. Illustration of the scattering matrix $S^{(i)}$ for an interface between medium i and vacuum. For the second medium on the receiving side, the incoming amplitude $b_{in}^{(i)}$ is zero.

and outgoing vacuum waves

$$[U_1^{(2)}, U_2^{(2)}, U_3^{(2)}, U_4^{(2)}, -U_{V-}] \begin{bmatrix} b_1^{(2)} \\ b_2^{(2)} \\ b_3^{(2)} \\ b_4^{(2)} \\ b_{V-} \end{bmatrix} = [-U_{in}^{(2)}, U_{V+}] \begin{bmatrix} b_{in}^{(2)} \\ b_{V+} \end{bmatrix}. \tag{D3}$$

By comparing Eqs. (D2) and (D3) with Eq. (D1), we obtain the expressions for the scattering matrices $S^{(1)}$ and $S^{(2)}$ as given in Eq. (13). Note that, even if we have formally used an input wave from medium (2) in the definition of $S^{(2)}$, due to the linearity of the problem it will not affect how an input wave from medium (1) is transmitted or reflected. In the actual computation of $S^{(2)}$ for the case of input wave from medium (1), $-U_{in}^{(2)}$ can be set arbitrarily, for example to zero.

APPENDIX E: DETAILS OF THE ANALYTICAL SOLUTION EXAMPLE

In the analytical example we presented in Sec. IV A, a hexagonal $6mm$ symmetry crystal was rotated in such way that its crystallographic c axis is aligned with the solid-vacuum interface and is perpendicular to the sagittal (incident) plane. The material parameters of the rotated crystal, ϵ^S the electric permittivity at constant strain, e the piezoelectric stress, and c^E the elastic stiffness at constant electric field, can be obtained using the method provided in Appendix F. To be specific, the crystal is rotated about the x axis by 90° following the right-hand rule, after which the rotated material tensors

read as

$$e = \begin{bmatrix} 0 & 0 & 0 & 0 & 0 & -e_{15} \\ -e_{31} & -e_{33} & -e_{31} & 0 & 0 & 0 \\ 0 & 0 & 0 & -e_{15} & 0 & 0 \end{bmatrix}, \tag{E1}$$

$$\epsilon^S = \begin{bmatrix} \epsilon_{11} & 0 & 0 \\ 0 & \epsilon_{33} & 0 \\ 0 & 0 & \epsilon_{11} \end{bmatrix}, \tag{E2}$$

$$c^E = \begin{bmatrix} c_{11} & c_{13} & c_{12} & 0 & 0 & 0 \\ c_{13} & c_{33} & c_{13} & 0 & 0 & 0 \\ c_{12} & c_{13} & c_{11} & 0 & 0 & 0 \\ 0 & 0 & 0 & c_{44} & 0 & 0 \\ 0 & 0 & 0 & 0 & c_{66} & 0 \\ 0 & 0 & 0 & 0 & 0 & c_{44} \end{bmatrix}. \tag{E3}$$

In Appendix B, the general approach for computing the extended Stroh 8×8 matrix N was described. However, this matrix can be significantly simplified in the analytical example in Sec. IV A. This is because, for this high-symmetry case, the piezoelectric response appears only along the crystal c axis, which is aligned with the y axis of the laboratory coordinates after the rotation [as shown in Fig. 2(a)], and there is no mode conversion as stated in the main text. Therefore, only the y -axis components, u_y in displacement and σ_{yz} in stress, enter the boundary conditions, Eqs. (6), and thus a reduced 4×4 Stroh matrix N and four-dimensional eigenvectors $\xi = [u_y, \phi, L_{yz}, D]^T$ are sufficient to solve the scattering problem at hand, involving only SH and E wave modes.

The explicit expression of the reduced Stroh matrix N is given in the main text in Eq. (17), and its eigenvalues and Stroh-normalized eigenvectors are

$$p_1 = -i, \quad \xi_1 = \left[0, \sqrt{\frac{i}{2\epsilon_{11}}}, \frac{e_{15}\sqrt{-i}}{\sqrt{2\epsilon_{11}}}, \frac{\sqrt{-i\epsilon_{11}}}{\sqrt{2}} \right]^T,$$

$$p_2 = i, \quad \xi_2 = \left[0, \frac{\sqrt{-i}}{\sqrt{2\epsilon_{11}}}, \frac{e_{15}\sqrt{i}}{\sqrt{2\epsilon_{11}}}, \frac{\sqrt{i\epsilon_{11}}}{\sqrt{2}} \right]^T,$$

$$p_3 = -\cot \theta_i, \quad \xi_3 = \left[\frac{\sqrt{2}}{2} \sqrt{\frac{k^2 \tan \theta_i}{\rho\omega^2}}, -\frac{\sqrt{2}e_{15}}{2\epsilon_{11}} \sqrt{\frac{k^2 \tan \theta_i}{\rho\omega^2}}, \frac{\sqrt{2}}{2} \sqrt{\frac{\rho\omega^2}{k^2 \tan \theta_i}}, 0 \right]^T,$$

$$p_4 = \cot \theta_i, \quad \xi_4 = \left[\frac{\sqrt{2}}{2} \sqrt{\frac{-k^2 \tan \theta_i}{\rho\omega^2}}, -\frac{\sqrt{2}e_{15}}{2\epsilon_{11}} \sqrt{\frac{-k^2 \tan \theta_i}{\rho\omega^2}}, \frac{\sqrt{2}}{2} \sqrt{\frac{-\rho\omega^2}{k^2 \tan \theta_i}}, 0 \right]^T.$$

The normalization conditions for the above solutions are $2(u_y L_{yz} + \phi D) = 1$, and the dispersion relation is $\rho\omega^2 = (c_{44} + e_{15}^2/\epsilon_{11})k^2$. The first two solutions (p_1, p_2) correspond to the two inhomogeneous E waves, and the last two (p_3, p_4) to the propagating SH waves.

APPENDIX F: CRYSTALLOGRAPHIC ORIENTATION

To solve the tunneling problem for an arbitrary crystal orientation, a method for transforming the material tensors from a standard crystallographic orientation to a specific arbitrary

rotation needs to be provided. The tensors in question are the electric permittivity at constant strain, ϵ_0^S , the piezoelectric stress, e_0 , and elastic stiffness at constant electric field, c_0^E , where the subscript 0 refers to the standard crystallographic orientation.

To describe the orientation of a crystal with respect to a fixed laboratory coordinate system, we adopt the Euler angle system [47]. In this system, we define two Cartesian frames XYZ and xyz , the crystal intrinsic coordinates and the external fixed laboratory coordinates, respectively. The relation between these two frames can be fully expressed by three angles: ϑ , φ , and ψ , as illustrated in Fig. 7(a).

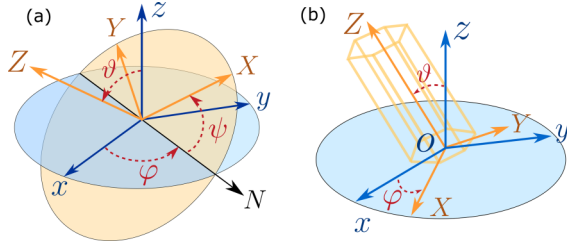


FIG. 7. Demonstration of crystal rotation angles. (a) The general Euler angle system. (b) The cylindrical angle system for uniaxial crystals

Several different conventions of the sequence of elemental rotations can be used to acquire the material constants for a specific crystal orientation $(\vartheta, \varphi, \psi)$. In this work, we adopted the widely used extrinsic z - x - z rotation sequence, which rotates the crystal frame from initial overlap with the laboratory coordinates to the desired orientation. In this procedure, the crystal frame will first be rotated about the z axis by an angle ψ defined by the right-hand rule (counterclockwise if viewed from top), followed by a second right-hand rotation of angle ϑ about the x axis, and finally a third right-hand rotation of angle φ about the z axis.

$$\mathbf{R}_{6,x}(\xi_x) = \begin{bmatrix} 1 & 0 & 0 & 0 & 0 & 0 & 0 & 0 & 0 \\ 0 & \cos^2(\xi_x) & \sin^2(\xi_x) & -2\sin(\xi_x)\cos(\xi_x) & 0 & 0 & 0 & 0 & 0 \\ 0 & \sin^2(\xi_x) & \cos^2(\xi_x) & 2\sin(\xi_x)\cos(\xi_x) & 0 & 0 & 0 & 0 & 0 \\ 0 & \sin(\xi_x)\cos(\xi_x) & -\sin(\xi_x)\cos(\xi_x) & -\sin^2(\xi_x) + \cos^2(\xi_x) & 0 & 0 & 0 & 0 & 0 \\ 0 & 0 & 0 & 0 & 0 & \cos(\xi_x) & \sin(\xi_x) & 0 & 0 \\ 0 & 0 & 0 & 0 & 0 & -\sin(\xi_x) & \cos(\xi_x) & 0 & 0 \end{bmatrix}, \quad (\text{F4})$$

$$\mathbf{R}_{6,z}(\xi_z) = \begin{bmatrix} \cos^2(\xi_z) & \sin^2(\xi_z) & 0 & 0 & 0 & -2\sin(\xi_z)\cos(\xi_z) & 0 & 0 & 0 \\ \sin^2(\xi_z) & \cos^2(\xi_z) & 0 & 0 & 0 & 2\sin(\xi_z)\cos(\xi_z) & 0 & 0 & 0 \\ 0 & 0 & 1 & 0 & 0 & 0 & 0 & 0 & 0 \\ 0 & 0 & 0 & \cos(\xi_z) & \sin(\xi_z) & 0 & 0 & 0 & 0 \\ 0 & 0 & 0 & -\sin(\xi_z) & \cos(\xi_z) & 0 & 0 & 0 & 0 \\ \sin(\xi_z)\cos(\xi_z) & -\sin(\xi_z)\cos(\xi_z) & 0 & 0 & 0 & -\sin^2(\xi_z) + \cos^2(\xi_z) & 0 & 0 & 0 \end{bmatrix}. \quad (\text{F5})$$

As a result, the material tensors are then obtained with the composite z - x - z rotation as

$$\begin{aligned} \epsilon^S &= \mathbf{R}_{3,z}(\varphi) \{ \mathbf{R}_{3,x}(\vartheta) [\mathbf{R}_{3,z}(\psi) \epsilon_0^S \mathbf{R}_{3,z}(\psi)^T] \mathbf{R}_{3,x}(\vartheta)^T \} \mathbf{R}_{3,z}(\varphi)^T, \\ \mathbf{e} &= \mathbf{R}_{3,z}(\varphi) \{ \mathbf{R}_{3,x}(\vartheta) [\mathbf{R}_{3,z}(\psi) \mathbf{e}_0 \mathbf{R}_{6,z}(\psi)^T] \mathbf{R}_{6,x}(\vartheta)^T \} \mathbf{R}_{6,z}(\varphi)^T, \\ \mathbf{c}^E &= \mathbf{R}_{6,z}(\varphi) \{ \mathbf{R}_{6,x}(\vartheta) [\mathbf{R}_{6,z}(\psi) \mathbf{c}_0^E \mathbf{R}_{6,z}(\psi)^T] \mathbf{R}_{6,x}(\vartheta)^T \} \mathbf{R}_{6,z}(\varphi)^T. \end{aligned} \quad (\text{F6})$$

For a solid with uniaxial symmetry about the crystal Z axis, such as in our example (the wurtzite hexagonal crystal ZnO), the first z -axis rotation will not change the material tensors. Thus for such a symmetry, the description of the orientation can be simplified from the Euler angle system to the cylindrical angle system, which uses only a zenith angle ϑ and an azimuthal angle φ , as shown in Fig. 7(b). The corresponding rotation transformations will also be reduced to a two-step procedure: first a right-hand rotation of ϑ about the x axis,

The material constant tensors (represented by $\mathbf{T}_{m \times n}$ matrices in the abbreviated index notation) can then be transformed to the rotated ones $\mathbf{T}'_{m \times n}$ by using rotation transformation matrices \mathbf{R} [3],

$$\mathbf{T}'_{m \times n} = \mathbf{R}_m \mathbf{T}_{m \times n} \mathbf{R}_n^T, \quad (\text{F1})$$

where \mathbf{R}_m or \mathbf{R}_n are the two rotation transformation matrices required for a general $m \times n$ matrix. In our case, ϵ_0^S has $m, n = 3$, \mathbf{e}_0 has $m = 3$ and $n = 6$, and \mathbf{c}_0^E has $m, n = 6$, so we need only two different dimensionalities of rotation matrices \mathbf{R}_3 and \mathbf{R}_6 for both the z and x axes, for a total of four rotation matrices.

For the crystal rotations about the x and z axes by the right-hand rule angles ξ_x and ξ_z , respectively, \mathbf{R}_3 can be expressed [3] as

$$\mathbf{R}_{3,x}(\xi_x) = \begin{bmatrix} 1 & 0 & 0 \\ 0 & \cos \xi_x & -\sin \xi_x \\ 0 & \sin \xi_x & \cos \xi_x \end{bmatrix}, \quad (\text{F2})$$

$$\mathbf{R}_{3,z}(\xi_z) = \begin{bmatrix} \cos \xi_z & -\sin \xi_z & 0 \\ \sin \xi_z & \cos \xi_z & 0 \\ 0 & 0 & 1 \end{bmatrix}. \quad (\text{F3})$$

\mathbf{R}_6 , required for the higher rank \mathbf{e} and \mathbf{c} tensors, can be obtained from the Bond stress matrix [3] as

followed by a second rotation of φ about the z axis. The material tensors will then be obtained as

$$\begin{aligned} \epsilon^S &= \mathbf{R}_{3,z}(\varphi) [\mathbf{R}_{3,x}(\vartheta) \epsilon_0^S \mathbf{R}_{3,x}(\vartheta)^T] \mathbf{R}_{3,z}(\varphi)^T, \\ \mathbf{e} &= \mathbf{R}_{3,z}(\varphi) [\mathbf{R}_{3,x}(\vartheta) \mathbf{e}_0 \mathbf{R}_{6,x}(\vartheta)^T] \mathbf{R}_{6,z}(\varphi)^T, \\ \mathbf{c}^E &= \mathbf{R}_{6,z}(\varphi) [\mathbf{R}_{6,x}(\vartheta) \mathbf{c}_0^E \mathbf{R}_{6,x}(\vartheta)^T] \mathbf{R}_{6,z}(\varphi)^T. \end{aligned} \quad (\text{F7})$$

APPENDIX G: WAVE-MODE ASSIGNMENT

Conventionally, there are two different approaches that have been widely used to categorize the three bulk elastic wave mode solutions. The first approach considers the relation between the particle displacement vector (also commonly known as the polarization vector) and the propagation direction of the wave (wave vector): when an elastic wave has a polarization that is (mostly) parallel to the propagating direction, it is identified as a (*quasi*-)longitudinal wave, or an L mode; if a transverse wave is polarized (mostly) inside the plane of incidence and (not purely) perpendicular to the propagation direction, it is a *vertically polarized* (*quasi*-)shear wave or an SV mode; and if a transverse wave is (mostly) perpendicular to both the plane of incidence and the propagation direction, it is a *horizontally polarized* (*quasi*-)shear or an SH mode. For anisotropic crystals, the quasiprefixes mostly apply, as pure L, SV, and SH polarizations appear only in certain high-symmetry propagation directions [3].

The second approach is to compare the phase velocities $v = \omega/k$ of the wave modes, and to designate the mode from the fastest to the slowest as (*quasi*-)longitudinal wave (L), *fast* (*quasi*-)transverse wave (FT), and *slow* (*quasi*-)transverse wave (ST).

It should be noted here that the choice for the categorization of the wave modes is a conceptual definition based on exactly the same set of solutions of the constitutive equations, and, therefore the choice of the categorization will not affect the results of the formalism discussed in this article. However, for completeness and for the benefit of the discussion of topics such as mode conversions, we provide here a procedure that can be programed to consistently identify the wave modes based on both categorization approaches in this work.

A total of eight eigenvalues p_α and their associated eigenvectors ξ_α can be obtained by solving the eigenfunction (3). In this section, we will examine these solutions with four different categorization methods:

- (1) homogeneous or inhomogeneous wave;
- (2) transmitted or reflected wave;
- (3) the mode categorized as longitudinal (L), fast transverse (FT), slow transverse (ST), or electric potential (E);
- (4) the mode categorized as longitudinal (L), vertically polarized shear (SV), horizontally polarized shear (SH), or electric potential (E).

The electric potential mode E is an inhomogeneous wave mode solution that appears in piezoelectric scattering problems (within the quasistatic approximation), describing a solution where the energy is mostly contained in the electric fields [3,48].

First, for a wave solution that has an eigenvalue $p_\alpha = p'_\alpha + ip''_\alpha$, we examine the imaginary part: If $p''_\alpha = 0$ ($p''_\alpha \neq 0$), the wave will be categorized as a homogeneous wave (an inhomogeneous wave).

Second, for an inhomogeneous wave, the scattering direction of the wave can be determined by the imaginary part of the eigenvalue: If $p''_\alpha > 0$ ($p''_\alpha < 0$) the wave will be categorized as a transmitted (reflected) wave. This follows from the principle that the physically allowed inhomogeneous wave

solution can only decay (and not grow) from the interface. In contrast, for a homogeneous plane wave, the direction of the power flow should be examined, as the normal components of the wave vector and the power flow can have different directions in general. By acknowledging the time-averaged Poynting vector in Eq. (5), a wave with $P_{n\alpha} < 0$ ($P_{n\alpha} > 0$) is categorized as a transmitted (reflected) wave.

The aforementioned wave modes (e.g., FT, SV, etc.) are defined from a partial set of characteristics of the wave solutions, such as phase velocity, polarization vector, etc. Therefore, it can in some cases be tricky to fully map such simplified mode definitions to the corresponding full solutions, and ambiguity can arise. For example, in some cases four scattered bulk modes can be excited simultaneously (without the excitation of the inhomogeneous E mode) due to a strong electromechanical coupling [48]. Therefore, it should be kept in mind that the mode categorization method presented here is not a fully robust and generally applicable algorithm.

To assign the modes within the set L, FT, ST, and E, we first compare the magnitudes of the imaginary parts $|p''_\alpha|$ of all the inhomogeneous evanescent waves ($p''_\alpha \neq 0$), and identify them based on the ordering $|p''_E| > |p''_L| > |p''_{FT}| \geq |p''_{ST}|$ (always starting from the E-mode, if fewer than four inhomogeneous modes exist). For the remaining unassigned homogeneous modes, the phase velocities $v_\alpha^2 = v_x^2/(1 + p_\alpha^2)$ will be examined, and the wave modes are assigned in the order $v_L^2 > v_{FT}^2 \geq v_{ST}^2$, starting from the first unassigned mode. This means that if, for example, the L mode was identified already as inhomogeneous, the fastest homogeneous mode would then be FT.

Finally, if one wishes to assign the modes within the set quasi-L, -SV, -SH, and -E, the polarization vectors A_α of the eigenvector solutions should be examined. However, we still first identify the inhomogeneous wave modes with the method described above, based on the magnitudes of the imaginary parts of the eigenvalues because there are often no clear general differences between the eigenvectors of the surface (inhomogeneous) modes.

In contrast, for the homogeneous modes, definitions based on the polarization vector exist. We identify them by comparing the polarization vector with the wave vector and the unit normal vector of the sagittal plane. If the quasi-L mode is still available for assignment, it can be identified from $|\mathbf{k} \cdot \mathbf{A}_L| > |\mathbf{k} \cdot \mathbf{A}_{SV,SH}|$. Within the coordinate system of this article, quasi-SV and quasi-SH modes can be identified from the relation $|[0, 1, 0]^T \cdot \mathbf{A}_{SV}| < |[0, 1, 0]^T \cdot \mathbf{A}_{SH}|$.

TABLE I. The common cut planes of hexagonal crystals: plane names, Miller indices, and rotation angles (ZnO).

Plane name	Miller index	$\angle_{\{hki\}}$
<i>a</i>	{11 $\bar{2}$ 0}	90°
<i>m</i>	{10 $\bar{1}$ 0}	90°
<i>c</i>	{0001}	0°
<i>r</i>	{1 $\bar{1}$ 02}	42.78°
<i>n</i>	{11 $\bar{2}$ 3}	46.89°
<i>s</i>	{10 $\bar{1}$ 1}	61.61°

APPENDIX H: COMMON CUT PLANES FOR A HEXAGONAL CRYSTAL

For hexagonal crystals, the four basis vector Miller-Bravais index system $\{hkil\}$ is commonly used to designate a crystallographic plane family [49]. These indices can be related to the crystal rotations, described in Sec. F, by $\vartheta = \angle_{\{hkil\}}$, in which $\angle_{\{hkil\}}$ is the angle between the plane normal and the crystal Z axis, and can be calculated from

$$\angle_{\{hkil\}} = \arccos \left(\frac{(\overrightarrow{hkl}) \cdot (\overrightarrow{001})}{|\overrightarrow{hkl}| |\overrightarrow{001}|} \right) = \arccos \left[al \left(\frac{4}{3} c^2 (h^2 + k^2 + hk) + a^2 l^2 \right)^{-\frac{1}{2}} \right],$$

where a and c are the in-plane (X, Y) and out-of-plane (Z) lattice constants of the crystal, respectively. The common crystallographic plane families for ZnO are given in Table I with their corresponding $\angle_{\{hkil\}}$.

-
- [1] D. Royer and E. Dieulesant, *Elastic Waves in Solids II, Generation, Acousto-Optic Interaction, Applications* (Springer-Verlag, Berlin, Heidelberg, 2000).
- [2] D. Royer and E. Dieulesant, *Elastic Waves in Solids I, Free and Guided Propagation* (Springer-Verlag, Berlin, Heidelberg, 2000).
- [3] B. A. Auld, *Acoustic Fields and Waves in Solids*, 2nd ed. (Krieger, Malabar, 1990).
- [4] B. V. Budaev and D. B. Bogy, On the role of acoustic waves (phonons) in equilibrium heat exchange across a vacuum gap, *Appl. Phys. Lett.* **99**, 053109 (2011).
- [5] Y. Ezzahri and K. Joulain, Vacuum-induced phonon transfer between two solid dielectric materials: Illustrating the case of Casimir force coupling, *Phys. Rev. B* **90**, 115433 (2014).
- [6] S. Xiong, K. Yang, Y. A. Kosevich, Y. Chalopin, R. D'Agosta, P. Cortona, and S. Volz, Classical to Quantum Transition of Heat Transfer between Two Silica Clusters, *Phys. Rev. Lett.* **112**, 114301 (2014).
- [7] V. Chiloyan, J. Garg, K. Esfarjani, and G. Chen, Transition from near-field thermal radiation to phonon heat conduction at sub-nanometre gaps, *Nat. Commun.* **6**, 6755 (2015).
- [8] J. B. Pendry, K. Sasihihlu, and R. V. Craster, Phonon-assisted heat transfer between vacuum-separated surfaces, *Phys. Rev. B* **94**, 075414 (2016).
- [9] A. I. Volokitin, Contribution of the acoustic waves to near-field heat transfer, *J. Phys.: Condens. Matter* **32**, 215001 (2020).
- [10] M. Balakirev, S. Bogdanov, and A. Gorchakov, Tunneling of an ultrasonic wave across a gap between lithium iodate crystals, *Fiz. Tverd. Tela (Leningrad)* **20**, 587 (1978) [*Sov. Phys. Solid State*, **20**, 338 (1978)].
- [11] M. Prunnila and J. Meltaus, Acoustic Phonon Tunneling and Heat Transport due to Evanescent Electric Fields, *Phys. Rev. Lett.* **105**, 125501 (2010).
- [12] S. Kaliski, The passage of an ultrasonic wave across a contactless junction between two piezoelectric bodies, *Proc. Vib. Probl. Warsaw* **7**, 95 (1966).
- [13] M. Balakirev and A. Gorchakov, Leakage of an elastic wave across a gap between piezoelectrics, *Fiz. Tverd. Tela (Leningrad)* **19**, 571 (1977) [*Sov. Phys. Solid State* **19**, 327 (1977)].
- [14] B. A. Auld, Wave propagation and resonance in piezoelectric materials, *J. Acoust. Soc. Am.* **70**, 1577 (1981).
- [15] D. M. Barnett and J. Lothe, Dislocations and line charges in anisotropic piezoelectric insulators, *Phys. Status Solidi B* **67**, 105 (1975).
- [16] J. Lothe and D. M. Barnett, Integral formalism for surface waves in piezoelectric crystals. existence considerations, *J. Appl. Phys.* **47**, 1799 (1976).
- [17] A. N. Stroh, Steady state problems in anisotropic elasticity, *J. Math. Phys. (Cambridge, Mass.)* **41**, 77 (1962).
- [18] P. Chadwick and G. D. Smith, Foundations of the theory of surface waves in anisotropic elastic materials, *Adv. Appl. Mech.* **17**, 303 (1977).
- [19] T. C. T. Ting, *Anisotropic Elasticity: Theory and Applications* (Oxford University Press, New York, 1996).
- [20] T. C. T. Ting, Recent developments in anisotropic elasticity, *Int. J. Solids Struct.* **37**, 401 (2000).
- [21] V. Al'shits, A. Darinskii, and A. Shuvalov, Theory of reflection of acoustoelectric waves in a semiinfinite piezoelectric medium. I. Metallized surface, *Kristallografiya* **34**, 1340 (1989) [*Sov. Phys. Crystallogr.* **34**, 808 (1989)].
- [22] V. Al'shits, A. Darinskii, and A. Shuvalov, Theory of reflection of acoustoelectric waves in a semiinfinite piezoelectric medium. II. Nonmetallized surface, *Kristallografiya* **35**, 7 (1990) [*Sov. Phys. Crystallogr.* **35**, 1 (1990)].
- [23] V. Al'shits, A. Darinskii, and A. Shuvalov, Theory of reflection of acoustoelectric waves in a semiinfinite piezoelectric medium. III. Resonance reflection in the neighborhood of a branch of outflowing waves, *Kristallografiya* **36**, 284 (1991) [*Sov. Phys. Crystallogr.* **36**, 145 (1991)].
- [24] M. Y. Chung and T. C. T. Ting, Line force, charge, and dislocation in anisotropic piezoelectric composite wedges and spaces, *J. Appl. Mech.* **62**, 423 (1995).
- [25] M. Akamatsu and K. Tanuma, Green's function of anisotropic piezoelectricity, *Proc. R. Soc. London, Ser. A* **453**, 473 (1997).
- [26] C. Hwu, Some explicit expressions of extended Stroh formalism for two-dimensional piezoelectric anisotropic elasticity, *Int. J. Solids Struct.* **45**, 4460 (2008).
- [27] V. N. Lyubimov, V. I. Al'shits, and J. Lothe, Body waves and quasi-body surface waves in a semi-infinite piezoelectric medium, *Kristallografiya* **25**, 33 (1980) [*Sov. Phys. Crystallogr.* **25**, 16 (1980)].
- [28] A. N. Darinskii and M. Weihnacht, Quasi-bulk surface and leaky waves in piezoelectrics of unrestricted symmetry, *Proc. R. Soc. London, Ser. A* **459**, 2977 (2003).
- [29] V. I. Al'shits, A. N. Darinskii, and A. L. Shuvalov, Acoustoelectric waves in bicrystal media in conditions of a rigid contact or a vacuum gap at an interface, *Kristallografiya* **38**, 22 (1993) [*Crystallogr. Rep.* **38**, 147 (1993)].

- [30] V. I. Al'shits, D. M. Barnett, A. N. Darinskii, and J. Lothe, On the existence problem for localized acoustic waves on the interface between two piezocrystals, *Wave Motion* **20**, 233 (1994).
- [31] A. N. Darinskii and M. Wehnacht, Gap acousto-electric waves in structures of arbitrary anisotropy, *IEEE Trans. Ultrason. Ferroelectr. Freq. Control* **53**, 412 (2006).
- [32] Y. V. Gulyaev and V. P. Plessky, Shear surface acoustic waves in dielectrics in the presence of an electric field, *Phys. Lett. A* **56**, 491 (1976).
- [33] Y. V. Gulyaev and V. P. Plesskii, Acoustic gap waves in piezoelectric materials, *Akust. Zh.* **23**, 716 (1977) [*Sov. Phys. Acoustics* **23**, 410 (1977)].
- [34] Y. E. Pak, Linear electro-elastic fracture mechanics of piezoelectric materials, *Int. J. Fract.* **54**, 79 (1992).
- [35] J. Liang, J. Han, B. Wang, and S. Du, Electroelastic modelling of anisotropic piezoelectric materials with an elliptic inclusion, *Int. J. Solids Struct.* **32**, 2989 (1995).
- [36] P. Lu, H. P. Lee, and C. Lu, Exact solutions for simply supported functionally graded piezoelectric laminates by stroh-like formalism, *Compos. Struct.* **72**, 352 (2006).
- [37] A. N. Darinskii and A. L. Shuvalov, Existence of surface acoustic waves in one-dimensional piezoelectric phononic crystals of general anisotropy, *Phys. Rev. B* **99**, 174305 (2019).
- [38] S. Benchabane, A. Khelif, J. Y. Rauch, L. Robert, and V. Laude, Evidence for complete surface wave band gap in a piezoelectric phononic crystal, *Phys. Rev. E* **73**, 065601(R) (2006).
- [39] A. N. Darinskii, On the theory of leaky waves in crystals, *Wave Motion* **25**, 35 (1997).
- [40] A. N. Darinskii, Leaky waves and the elastic wave resonance reflection on a crystal-thin solid layer interface. ii. leaky waves given rise to by exceptional bulk waves, *J. Acoust. Soc. Am.* **103**, 1845 (1998).
- [41] D. Polder and M. Van Hove, Theory of radiative heat transfer between closely spaced bodies, *Phys. Rev. B* **4**, 3303 (1971).
- [42] J. B. Pendry, Radiative exchange of heat between nanostructures, *J. Phys.: Condens. Matter* **11**, 6621 (1999).
- [43] K. Joulain, J.-P. Mulet, F. Marquier, R. Carminati, and J.-J. Greffet, Surface electromagnetic waves thermally excited: Radiative heat transfer, coherence properties and Casimir forces revisited in the near field, *Surf. Sci. Rep.* **57**, 59 (2005).
- [44] K. Malén and J. Lothe, Explicit expressions for dislocation derivatives, *Phys. Status Solidi B* **39**, 287 (1970).
- [45] I. N. Court and F. K. von Willisen, Frustrated total internal reflection and application of its principle to laser cavity design, *Appl. Opt.* **3**, 719 (1964).
- [46] M. Born and E. Wolf, *Principles of Optics*, 7th ed. (Cambridge University Press, Cambridge, 1999).
- [47] H. Goldstein, *Classical Mechanics*, 2nd ed. (Addison-Wesley Publishing, Reading, 1980).
- [48] A. G. Every and V. I. Neiman, Reflection of electroacoustic waves in piezoelectric solids: Mode conversion into four bulk waves, *J. Appl. Phys.* **71**, 6018 (1992).
- [49] D. Schwarzenbach, Note on Bravais-Miller indices, *J. Appl. Crystallogr.* **36**, 1270 (2003).